Nano Energy 149 (2026) 111731

Contents lists available at ScienceDirect

Nano Energy

journal homepage: www.elsevier.com/locate/nanoen

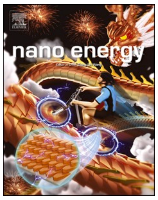

The role of oxygen vacancies: Triggering lattice oxygen oxidation mechanism in acidic OER

Qiang Fu [a,1], Lok Wing Wong [a,1], Xiaodong Zheng [a], Chi Shing Tsang [a], Honglin Chen [a], Wenqian Shen [a], Tao Ling [b], Thuc Hue Ly [c,d,e,*], Qingming Deng [f,**], Jiong Zhao [a,g,***]

[a] Department of Applied Physics, The Hong Kong Polytechnic University, Kowloon, China
[b] Key Laboratory for Advanced Ceramics and Machining Technology of Ministry of Education, Institute of New Energy, School of Materials Science and Engineering, Tianjin University, Tianjin 300072, China
[c] Department of Chemistry and Center of Super-Diamond & Advanced Films (COSDAF), City University of Hong Kong, Kowloon, China
[d] Department of Chemistry and State Key Laboratory of Marine Environmental Health, City University of Hong Kong, Hong Kong, China
[e] City University of Hong Kong Shenzhen Research Institute, Shenzhen, China
[f] Physics Department and Jiangsu Key Laboratory for Chemistry of Low-Dimensional Materials, Huaiyin Normal University, Huaian 223300, China
[g] The Hong Kong Polytechnic University Shenzhen Research Institute, Shenzhen 518055, China

ARTICLE INFO

Keywords:
Spinel oxides
Electrocatalysis
Oxygen vacancy
Acidic oxygen evolution reaction
Lattice oxygen

ABSTRACT

Rational design of highly efficient, acid-stable electrodes for oxygen production is crucial in the development of proton exchange membrane (PEM) electrolyzers. Spinel oxides have recently been discovered as effective catalysts for oxygen evolution reaction (OER), owing to their moderate adsorption energy of reaction intermediates. In this study, we present our findings that the incorporation of oxygen vacancies (O_V) into spinel oxides could enable a switch from the inefficient adsorbate evolution mechanism (AEM) to the highly efficient lattice-oxygen oxidation mechanism (LOM) for OER. We show that oxygen vacancies promote OER mechanism transitions in oxide electrocatalysts while maintaining stable catalytic performance. These results provide important insight into the role of elemental doping in regulating reaction pathways under acidic conditions. The representative Mn/Ru-Co_3O_4 catalyst can reach an impressive low overpotential of 230 mV to deliver a current density of 10 mA cm^{-2}, which is ~ 48 % lower than the pristine Co_3O_4. Theoretical calculations reveal O_V around the active sites could lower the energy barrier in the rate-determining step and prevent the formation of *OOH species. As a result, this process disrupts the scaling relationship observed in traditional AEM mechanisms, leading to a substantial enhancement in overall catalytic activity.

1. Introduction

The acidic oxygen evolution reaction (OER) remains a significant bottleneck in proton exchange membrane water electrolysis (PEMWE), which is a promising technology for future clean energy production due to its low ohmic losses and high current density [1–5]. However, the corrosive nature of the electrolyte restricts the selection of electrodes and catalysts to noble metals such as Pt, Ir, and Ru, resulting in significantly higher production costs [6]. Recently, a new class of materials called spinel oxides, including Co_3O_4, Mn_3O_4, and others, has emerged as potential candidates for acidic OER electrocatalysts [2,7–9]. Despite their potential, spinel oxides exhibit relatively weak intrinsic catalytic activity, necessitating the incorporation of heavy loads of noble metals to achieve satisfactory catalytic performance (Table S1). To optimize the catalytic mechanism of spinel oxides for acidic OER [10], a more comprehensive analysis of the reaction mechanism is required.

Regarding acidic OER, a newly proposed lattice oxygen mechanism (LOM) has recently proved to be more efficient than the widely accepted adsorbate evolution mechanism (AEM) [11–13]. For the AEM, the OER process involves multiple oxygen-containing intermediates, including *OH, *O, and *OOH. Theoretical calculation results suggested that the binding energies of the intermediates *OH and *OOH are correlated and

---

* Corresponding author at: Department of Chemistry and Center of Super-Diamond & Advanced Films (COSDAF), City University of Hong Kong, Kowloon, China.
** Corresponding author.
*** Corresponding author at: Department of Applied Physics, The Hong Kong Polytechnic University, Kowloon, China.
E-mail addresses: thuchly@cityu.edu.hk (T.H. Ly), q.deng@hytc.edu.cn (Q. Deng), jiongzhao@polyu.edu.hk (J. Zhao).
[1] These authors contributed equally.

https://doi.org/10.1016/j.nanoen.2026.111731
Received 24 November 2025; Received in revised form 26 December 2025; Accepted 14 January 2026

follow the scaling relationship with the free energy difference of $\Delta G_{*OOH} = \Delta G_{*OH} + 3.2 \pm 0.2$ eV. This relationship implies that the optimization of the adsorption of these two intermediate products on the catalytic active site cannot be achieved individually, and the predicted lowest overpotential (η) is ~370 ± 100 mV [14–16]. In contrast, in the LOM, after the deprotonation of the first adsorbed *OH, the *O intermediate directly couples with the activated lattice oxygen around the active sites. Since no *OOH species is formed, the scaling relationship pathway is broken, which results in a lower η than the theoretical limit in AEM mechanism [15,17,18].

With LOM proposed to be more efficient for acidic OER, there are still critical challenges in the rational design of electrocatalysts that predominantly follow the LOM [19,20]. One of these challenges is related to the stability of the materials. In the LOM, the lattice oxygen atom actively participates in the catalytic process. As a result, the formation of further oxygen vacancies (O_V) can occur, which may render the metal active sites more susceptible to dissolution into the electrolyte, especially in acidic media [21]. The lack of stability poses a significant obstacle in the development of electrocatalytic materials that can sustain long-term performance under the harsh conditions of acidic OER.

Furthermore, the exact origin of the LOM remains unclear, and the transition from AEM to the highly efficient LOM is uncontrollable. In previous studies, elemental doping was often considered as a method to enhance the stability of materials and facilitate the transition in catalytic mechanisms. For instance, Mn, among the transition metal elements, is known for its ability to remain stable during the acidic OER process [22,23], and its self-repairing functionality is believed to contribute to stronger metal bonding in catalytic systems, thereby enhancing their overall stability. However, when used alone, Mn-based catalysts [24–26] exhibit lower OER activity compared to Co-based catalysts [7,27,28]. Therefore, Mn-based catalysts are often employed as stabilizers in catalytic systems [29]. It is even possible to create a synergistic effect between the enhanced stability from Mn and the improved OER activity from Co-based catalysts [2,23]. Furthermore, the transition of catalytic mechanisms through doping with heteroatoms has shown promise in certain cases. However, doping may not consistently achieve a mechanism transition, even within similar material systems [9,17,30–33].

In this work, we have developed a Mn/Ru co-doped Co_3O_4 (Mn/Ru-Co_3O_4) spinel oxide catalyst for acidic OER, combining the stability of Mn and the high catalytic activity of Ru. Detailed characterizations and theoretical calculation results have revealed the distinct and synergistic roles of O_V and elemental doping in promoting the acidic OER performance of spinel oxides. We identified that O_V, as well as doping, are the key factors for AEM to LOM transition in spinel oxides. Density functional theory (DFT) calculation results further reveal that the transition in the reaction mechanism stems from the increased difficulty in generating OOH species, thereby effectively lowering the energy barrier for the rate-determining step. As a result, the Co-doped Mn/Ru-Co_3O_4 demonstrated a relatively low overpotential (η_{10}) of 230 mV vs. RHE to deliver a current density of 10 mA cm^{-2} in 0.5 M H_2SO_4 and can steadily operate for more than 120 h, which is superior to the majority of reported spinel oxides used in acidic OER reactions. These findings will provide valuable insights into the rational design of electrocatalysts and enable controllable modulation of the catalytic mechanism for the acidic OER.

2. Results and discussions

2.1. Characterizations

Co_3O_4 is a typical cubic phase spinel oxide (space group: $Fd\overline{3}m$) with two kinds of Co ions: one Co^{2+} ion is embedded into a tetrahedral site, while two Co^{3+} are located in the center of octahedral sites (denoted as Co_{Tet}, and Co_{Oct}, respectively) [28]. As shown in Fig. 1a, the Co atoms are connected with two different styles, i.e., the corner-shared Co_{Tet}-Co_{Oct} (with a distance of ~3.35 Å) and the edge-shared Co_{Oct}-Co_{Oct} (with a distance of ~2.85 Å). These diverse coordination structures provide Co_3O_4 and other similar spinel oxides with a wide range of controllable spaces when serving as OER electrocatalysts [34].

In this study, we successfully synthesized spinel Co_3O_4 and its doped variants, namely Mn-Co_3O_4 (Mn doped sample), Ru-Co_3O_4 (Ru doped sample), and Mn/Ru-Co_3O_4 (Mn/Ru co-doped sample) (see Methods). The crystal structures of the as-prepared samples were first thoroughly investigated with transmission electron microscopy (TEM) techniques. The high-resolution TEM (HRTEM) image of the Mn/Ru-Co_3O_4 nanosheets (NSs) demonstrated two noticeable lattice fringes belonging to the (111) plane (4.66 Å) and ($2\overline{2}0$) plane (2.89 Å), respectively (Figure S1a). The corresponding selected area electron diffraction (SAED) pattern clearly demonstrated the polycrystalline nature of the synthesized sample (Figure S1b). High-angle annular dark-field scanning transmission electron microscope (HAADF-STEM) image and the corresponding energy dispersive spectroscopy (EDS) mapping of the representative Mn/Ru-Co_3O_4 NSs exhibited hexagonal porous morphology, with all elements uniformly distributed within the NSs (Figure S1c). The doping amount of Mn and Ru were 2.9 at% and 8.1 at %, respectively, according to the EDS spectra (Figure S2 and Table S2).

Since the electrocatalysis process is basically a surface reaction, the exposed surfaces would demonstrate significant influence on the final catalytic performances and the explanation of the corresponding mechanism. In order to understand the precise atomic structures of the exposed crystal facets, we conducted a statistical analysis of the potentially exposed crystal facets using the aberration-corrected HAADF-STEM technique. Some typical images of different positions of the Mn/Ru-Co_3O_4 NSs are demonstrated in Figure S3. After performing statistics on the length of the exposed surfaces, we have determined that the {022}, {113} and {111} planes are the three dominant planes that exposed on surfaces (Figure S4). These surface planes will serve as the basis for further analysis.

The integrated differential phase contrast scanning transmission electron microscopy (iDPC-STEM) technique was employed for further confirmation of the doping sites of the heavy Ru atom and the presence of Ov. Atomic-resolution iDPC-STEM images were acquired along the [211], [233], and [110] zone axes, with {022}, {113}, and {111} being the observed exposed surfaces, respectively (Fig. 1b to 1d). The line profile analysis of each zone axis demonstrated relatively strong intensity at specific atom sites, which should be attributed to the heavy Ru atom (Fig. 1e to 1g). Based on further analysis using the crystal structure characteristics of different zone axes and the simulation results from HAADF-STEM images, it was found that Ru tends to occupy the octahedral cobalt (Co_{Oct}) sites as the preferred substitution site (Figure S5). Regarding the doped Mn atoms, as both HAADF-STEM and iDPC-STEM techniques rely on atomic weight (atomic number) for imaging, those atoms with similar atomic numbers (such as Mn and Co) do not exhibit significant intensity differences. Therefore, additional characterization techniques were employed to determine the doping position of Mn, which will be presented and discussed in the following analysis.

We further analyzed the presence of O_V according to the iDPC-STEM image obtained from the [110] zone axis (Fig. 1h). Line profile along the O atom columns from P1 to P8 was demonstrated in Fig. 1i. According to the variation in line profile intensity, it could be concluded that O_V existed at the positions P5-P7, which demonstrated that O_V was commonly present in samples prepared with liquid-phase reactions involved synthesis strategies. For other samples (Co_3O_4, Mn-Co_3O_4, and Ru-Co_3O_4), the corresponding HRTEM images, SAED patterns, and EDS spectra were exhibited in Figure S6 to S11, which showed that all the samples were well-crystallized, and the content of each single doped component is consistent with the specific component content in the co-doped samples.

Next, electron energy loss spectroscopy (EELS) was employed to probe local electronic structure variations at the surface and near-

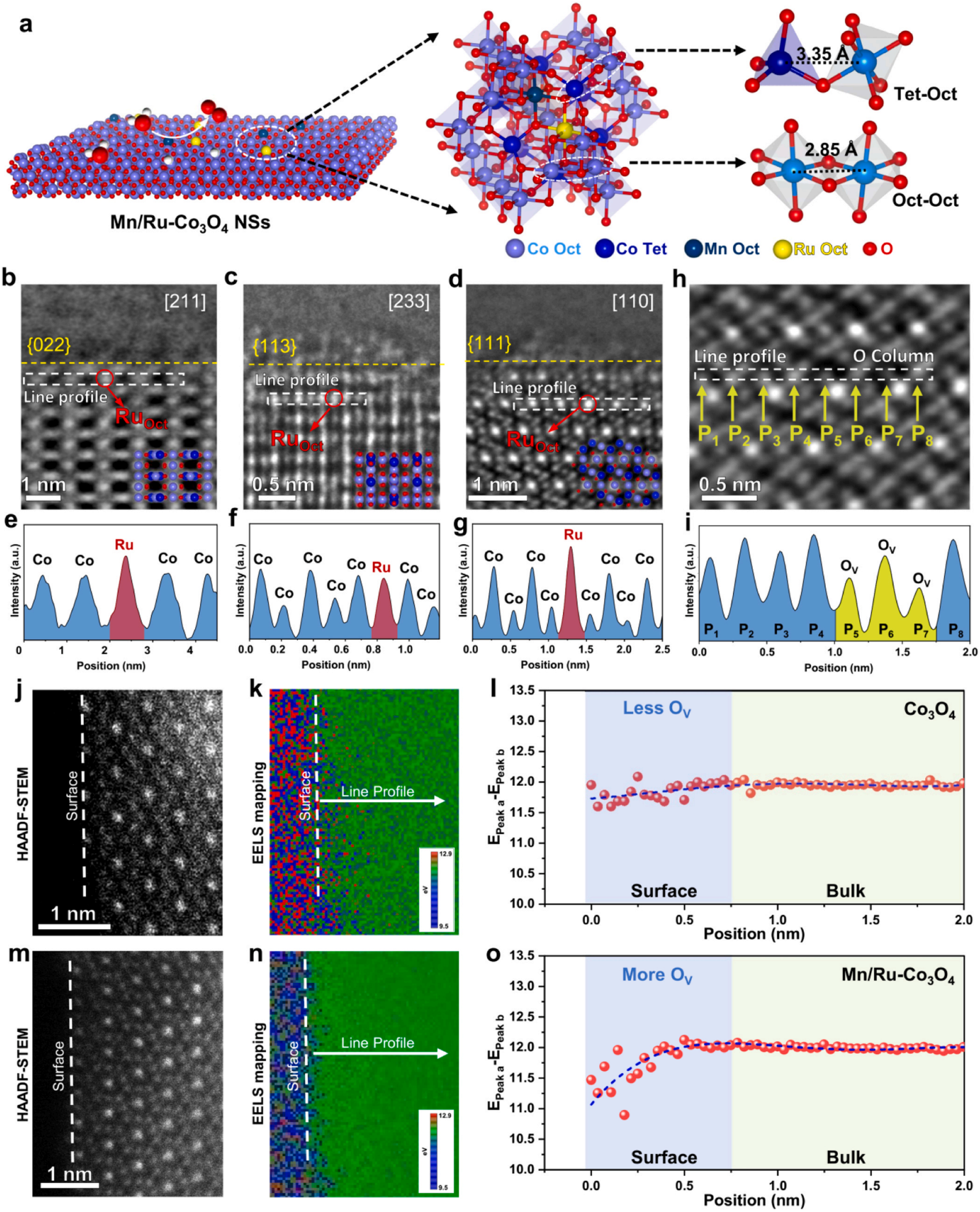

Fig. 1. Atomic-scale structural analysis of Mn/Ru-Co$_3$O$_4$ sample. a Schematic illustration of the crystal structure of spinel Mn/Ru-Co$_3$O$_4$. Atomic-resolution iDPC-STEM images were captured along b [211], c [233], and d [110] zone axis and the corresponding line profile in e, f, and g, which clearly confirmed the Ru atoms were doped into the octahedral sites. h iDPC-STEM image obtained along [110] zone demonstrated the presence of O$_V$. i Intensity line profiles alone the dashed box in h, and the lower intensity at P$_5$-P$_7$ indicated the presence of O$_V$. j HAADF-STEM image of Co$_3$O$_4$, and k the corresponding EELS mapping of the peak position difference for peak *a* and peak *b*. l The intensity line profile along the line in k. m HAADF-STEM image of Mn/Ru-Co$_3$O$_4$, and n the corresponding EELS mapping of the peak position difference for peak *a* and peak *b*. o The intensity line profile along the line in n.

surface regions. For Mn/Ru-Co_3O_4, the Co L-edge EELS line-scan reveals a slightly increased L_3/L_2 intensity ratio at the surface compared with the bulk region (Figure S12), whereas pristine Co_3O_4 exhibits nearly identical L_3/L_2 ratios across the entire particle (Figure S13). Such a surface-localized increase in the L_3/L_2 ratio indicates a reduced average Co valence state, which is commonly associated with oxygen-deficient environments [35,36]. To further examine oxygen-related electronic structure changes, spatially resolved O K-edge EELS mapping was performed. Compared with pristine Co_3O_4 (Fig. 1j-l), the Mn/Ru- Co_3O_4 sample shows a reduced energy separation between peak a (~531 eV) and peak b (~543 eV) in the near-surface region (Fig. 1m-o). This contraction of the O K-edge feature separation reflects weakened metal-oxygen hybridization and a reduced oxygen coordination environment, consistent with enhanced oxygen deficiency at the surface [37, 38]. These results further proved that elemental doping can facilitate the formation of O_v, which may have some significant influence on the overall electrochemical activities of Mn/Ru-Co_3O_4.

2.2. *Characterizations on macro-scale*

To achieve a complete understanding of the as-synthesized samples, X-ray absorption spectroscopy (XAS) was applied to further analyze the coordination structure of the representative Mn/Ru-Co_3O_4. X-ray absorption near edge structure (XANES) spectra of Co K-edge demonstrated that, after Mn/Ru co-doping, the adsorption edge of Co slightly shifted to higher energy, indicating a slightly higher oxidation state of Co atom compared with pristine Co_3O_4 (Fig. 2a). Further fitting showed that the average oxidation state of Co atom in Mn/Ru-Co_3O_4 is about + 2.88, while the theoretical average valence state (+2.67) (Figure S14a). Similar analysis for Mn and Ru (Fig. 2b and 2c) indicated the oxidation state of Mn and Ru were +3.72 and +3.43, respectively (Figure S14b and S14c).

The local coordination structure is of crucial importance for elucidating the origin of catalytic activity. As mentioned earlier, the precise doping position of Ru atoms has been identified as the octahedral sites according to the HAADF-STEM images. However, it is challenging to determine the exact position of Mn atoms from the atomic resolution STEM images. Thus, we further investigated the local coordination structure of the metal cations in Mn/Ru-Co_3O_4 with extended X-ray absorption fine structure (EXAFS) spectroscopies. The EXAFS spectrum of Co K-edge demonstrated three distinct peaks, belonging to Co-O scattering (1.53 Å), Co-M_{Oct} scattering (M_{Oct} response to Co, Mn, or Ru atoms at octahedral sites, with a distance of about 2.49 Å), and Co-M_{Tet} scattering (M_{Tet} response to Co, Mn, or Ru atoms at tetrahedral sites, with a distance of about 3.1 Å) (Fig. 2d). For the Mn K-edge EXAFS spectra, there are also three characteristic peaks located at 1.47 Å, 2.49 Å, and 3.2 Å, which belonged to the Mn-O scattering, Mn-M_{Oct} scattering, and Mn-M_{Tet} scattering (Fig. 2e). As mentioned in Fig. 1a, there are two different coordination structures in spinal Co_3O_4. If the Mn atom was doped into the tetrahedral sites, it would result in a corner shared coordination structure with the neighboring coordinating metal atoms, and the distance was about 3.3 Å, which clearly contradicted our EXAFS results of Mn K-edge. Considering the existence of the strong Mn-M_{Oct} scattering peak and the relatively weak Mn-M_{Tet} signal, it could be

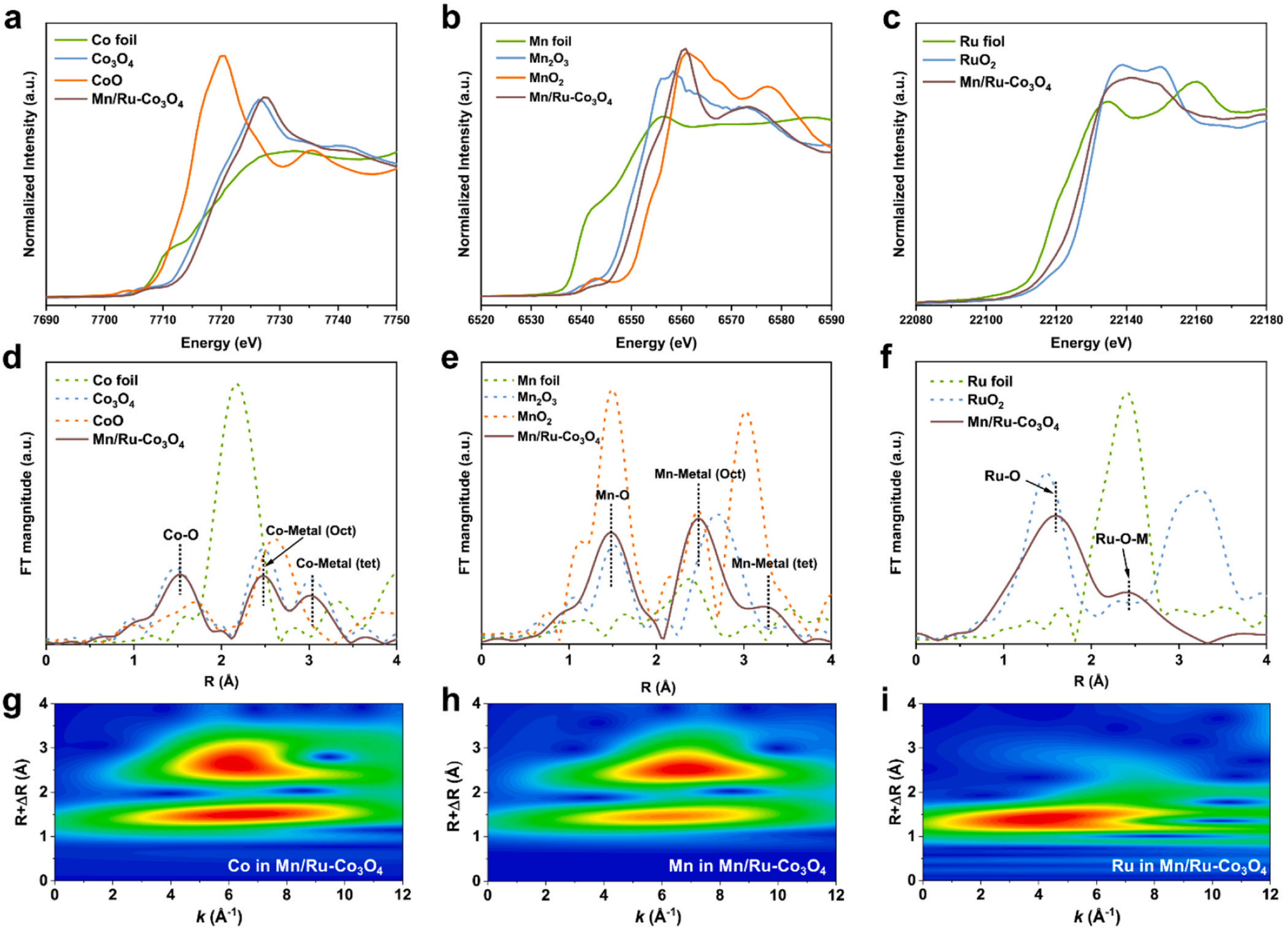

Fig. 2. Coordination analysis of Mn/Ru-Co_3O_4. K-edge XANES spectra of a Co, b Mn, and c Ru in Mn/Ru-Co_3O_4. *K*-edge k^3-weighted Fourier transform (FT) spectra of d Co, e Mn, and f Ru, and g-i demonstrated the corresponding WT of the k^3-weighted EXAFS signals.

concluded that the doped Mn atoms preferentially substituted the octahedral sites in the Co_3O_4 matrix. Ru K-edge EXAFS demonstrated two prominent peaks located at 1.6 Å and 2.4 Å, which belonged to the Ru-O and Ru-M_{Oct} scattering (Fig. 2f), which consisted well with the fitting results (Figure S15 and Table S3). Therefore, based on the combined results of HAADF-STEM and XAS, it could be concluded that Mn and Ru atoms would both primarily substitute the Co_{Oct} sites in Co_3O_4, which is further proved by the wavelet-transform (WT)-EXAFS analyses for Co, Mn and Ru (Fig. 2g to 2i).

To further characterize the crystal and chemical state of the as-prepared samples, various spectroscopic techniques were employed, including Powder X-ray Diffraction (PXRD), Raman spectroscopy, Electron Paramagnetic Resonance (EPR), X-ray Photoelectron Spectroscopy (XPS), PXRD patterns demonstrated that all samples were typical cubic phase Co_3O_4 (JCPDS #71–0816), indicating the doping of heteroatoms does not significantly affect the crystal configuration of the matrix Co_3O_4 (Fig. 3a). Raman spectra of different samples demonstrated similar five characteristic peaks located at around 189.7 cm^{-1} (F_{2g}), 468.4 cm^{-1} (E_g), 511.4 cm^{-1} (F_{2g}), 606.7 cm^{-1} (F_{2g}), and 674.5 cm^{-1} (A_{1g}) (Fig. 3b) [7]. Compared with pristine Co_3O_4, the modified samples display a slight redshift of the A_{1g} mode from 674.5 cm^{-1} to 669.2 cm^{-1}, indicating oxygen-related local structural evolution within the spinel lattice. Such a shift can be attributed to the combined effects of oxygen vacancy formation and subtle Co-O bond perturbations associated with lattice oxygen activation, reflecting a modified local oxygen coordination environment. In addition to the peak position shift, a moderate broadening of the A_{1g} mode is also observed after vacancy engineering and elemental doping. The slightly increased full width at half maximum (FWHM) suggests the introduction of localized structural disorder, which is consistent with the formation of oxygen-defective regions and heteroatom-induced lattice perturbations. Notably, the extent of peak broadening remains limited, indicating that the induced disorder is confined and does not lead to severe lattice distortion or phase transformation [39,40]. The increase of O_V concentration after heteroatom doping was further confirmed by the EPR spectra (Fig. 3c). The characteristic signal at g=2.002 appeared in the spectra of all samples, indicating the presence of unavoidable O_V during the synthesis process. However, after doping heteroatoms, the signal intensity gradually increased, in consistent with the trend observed in the Raman spectra.

Then, XPS spectra were applied to investigate the surface chemical state of each sample. For Co atoms in matrix Co_3O_4, the Co $2p_{3/2}$ could be deconvoluted into three different peaks located at ~779.4 eV (Co^{3+}), ~780.9 eV (Co^{2+}), and ~780.0 eV (satellite peak), as demonstrated in Fig. 3d [8,31]. It exhibited that doping with Mn and Ru would slightly increase the oxidation state of Co, which indicated the redistribution around Co atoms (Fig. 3d). However, when Mn and Ru were co-doped into Co_3O_4, the oxidation states were reduced to levels close to the

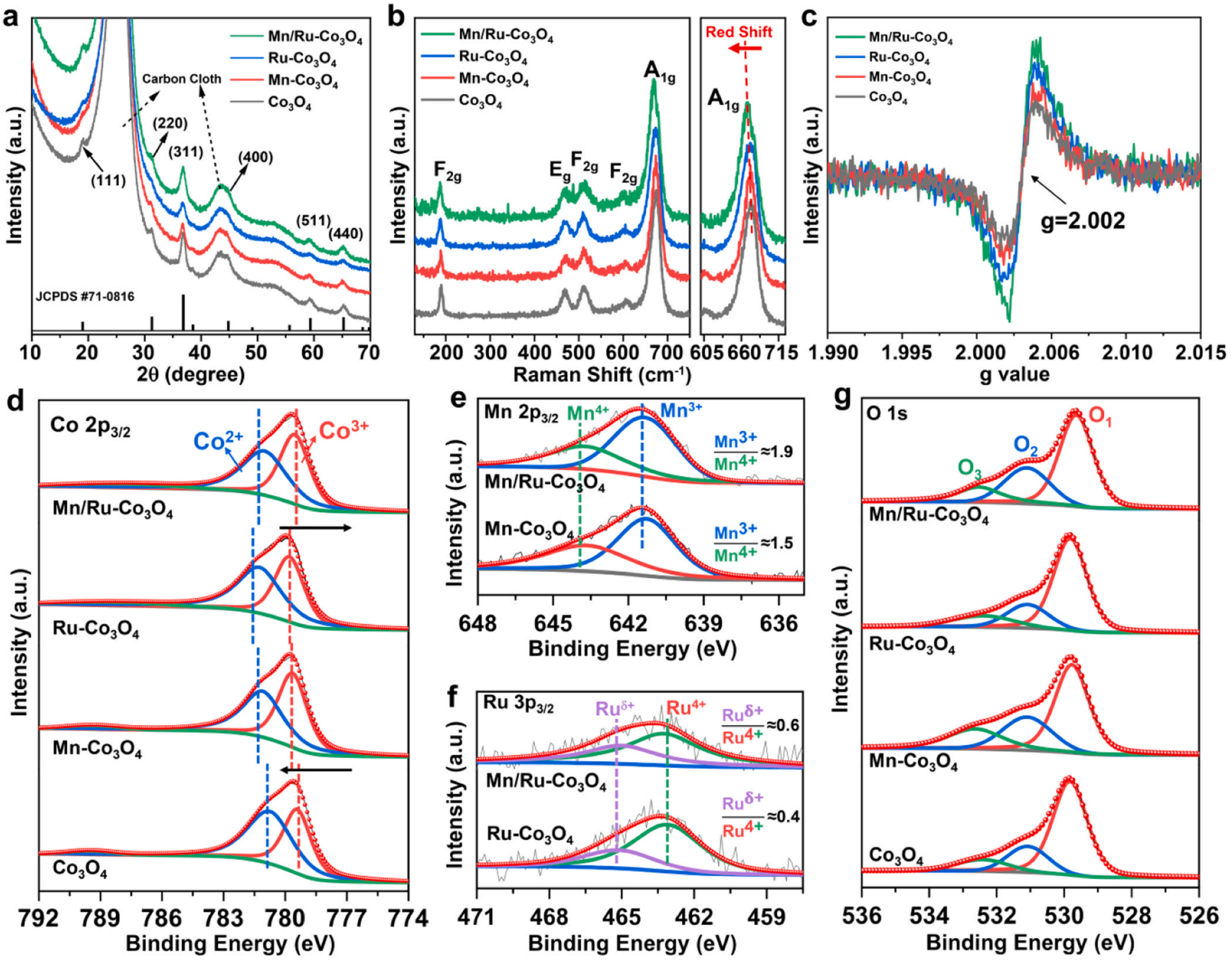

Fig. 3. Spectral characterizations for different samples. a PXRD patterns and b Raman spectra for the as-synthesized samples. c EPR signal of O_V in different samples. XPS spectra of d Co $2p_{3/2}$, e Mn $2p_{3/2}$, f Ru $3p_{3/2}$, and g O 1 s core-level with peak fitting results.

pristine state. This suggested a more vital interaction between Mn and Ru, leading to a reduction state of Co atoms at the surfaces, which is in accordance with our previous EELS results. Dual atom doping allowed for the increase of active sites while also ensuring that the matrix Co_3O_4 maintained a lower oxidation state. This not only guarantees catalytic activity but also preserves the stability of the matrix material, reducing the activity decay caused by Co leaching [29].

In the comparative analysis of Mn $2p_{3/2}$[41] and Ru $3p_{3/2}$[42] spectra, it was found that the oxidation state of Mn atom would undergo a reduction process (Mn^{3+}/Mn^{4+} ratio increased from 1.5 to 1.9), while the oxidation state of Ru would increase accordingly ($Ru^{\delta+}/Ru^{4+}$ increased from 0.4 to 0.6, $\delta>4$). The valence variation of Mn and Ru further revealed the pronounced interaction between Mn and Ru, and the electrons would transfer from Ru to the nearby Mn (Fig. 3e and 3f). Due to Mn being one of the few non-precious metal elements that exhibit stability under acidic OER conditions, the interaction established between Mn and Ru is expected to contribute to stabilizing the Ru atoms during the reaction process [2,24,43]. Simultaneously, with the observed increase in the oxidation state of Ru, it becomes more prone to oxidation to higher oxidation state states when acting as reactive sites, thereby enhancing the overall reactivity [3,44,45].

The XPS deconvolution results indicate that the O_V content in the

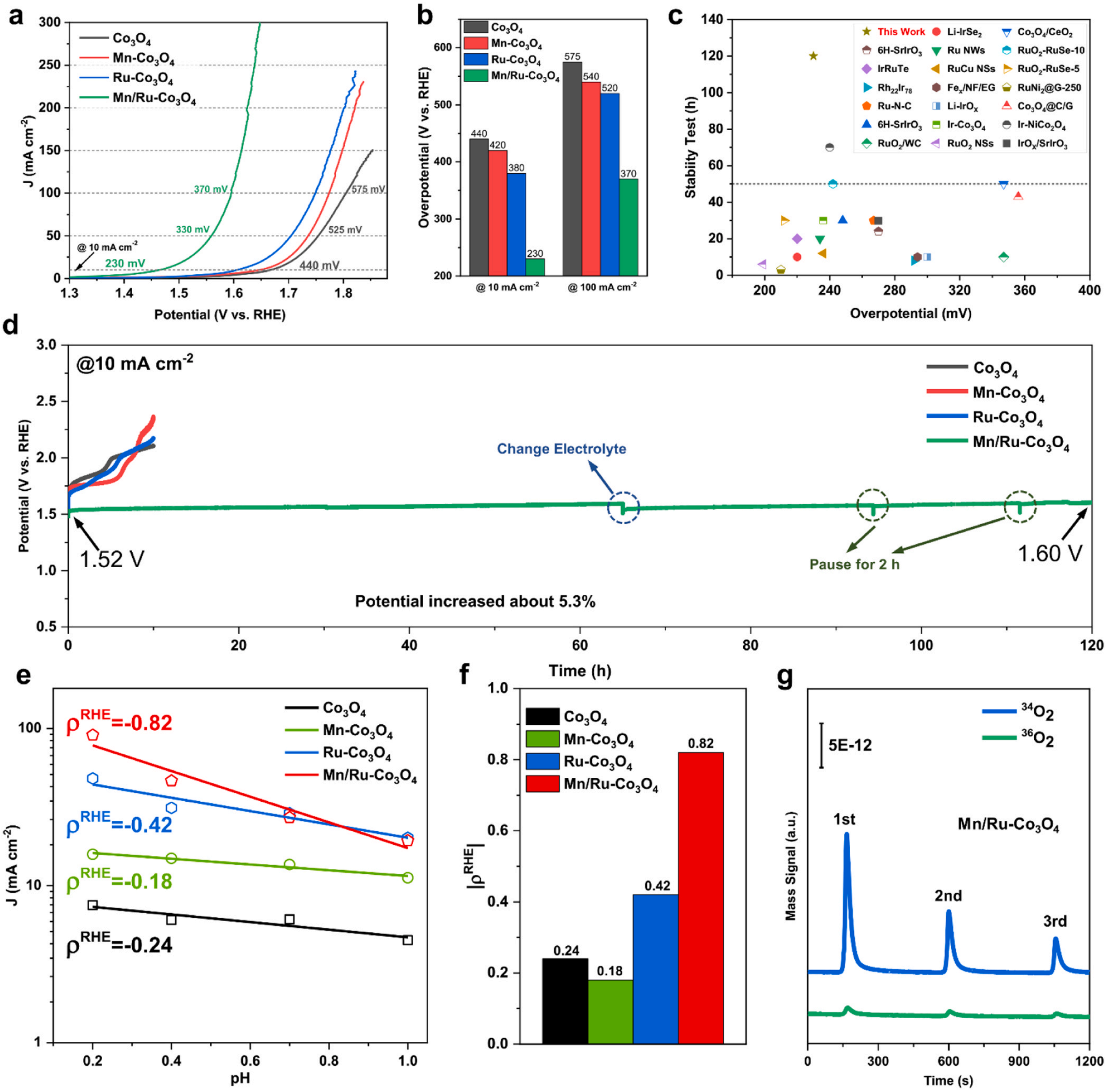

Fig. 4. Acidic OER performances of different samples. a LSV curves of four reprehensive samples in 0.5 M H_2SO_4. b Overpotential for different samples to deliver current densities of 10 mA cm^{-2} and 100 mA cm^{-2}. c Comparisons of overpotentials and stabilities of related electrocatalysts and Mn/Ru-Co_3O_4 NSs. d Acidic OER stability test of four different samples. e Current densities of different samples obtained at 1.65 V vs. RHE plotted in log scale as a function of pH. f The proton reaction orders ($\rho^{RHE} = \partial logi/\partial pH$) acquire from e for each sample. g DEMS measurements of ^{34}O ($^{16}O^{18}O$) and ^{36}O ($^{18}O^{18}O$) signals from the reaction products for ^{18}O-labeled Mn/Ru-Co_3O_4 in 0.5 M H_2SO_4 in $H_2^{16}O$.

$Mn/Ru-Co_3O_4$ sample increased to 27.4 % compared to 20.0 % in undoped Co_3O_4, consistent with Raman and EPR analyses. The detailed distribution of oxygen species shows that lattice oxygen (O_1), oxygen vacancies (O_2), and adsorbed oxygen (O_3) account for 68.5 %, 20.0 %, and 11.5 % in Co_3O_4; 65.4 %, 21.1 %, and 13.5 % in $Mn-Co_3O_4$; 53.9 %, 26.0 %, and 20.1 % in $Ru-Co_3O_4$; and 57.9 %, 27.4 %, and 14.7 % in $Mn/Ru-Co_3O_4$, respectively. These results further support that doping is an effective strategy to increase the O_V ratio and tune the surface oxygen chemistry (Table S4).

2.3. Evaluation of electrochemical activities

The acidic OER activities for different samples were evaluated in 0.5 M H_2SO_4 (see Methods for more details). The linear sweep voltammetry (LSV) curves of the four representative samples demonstrated $Mn/Ru-Co_3O_4$ required an overpotential (η_{10}) of 230 mV to deliver a current density of 10 mA cm^{-2} (Fig. 4a, and Table S5), surpassing the performance of the other control samples (Fig. 4b and Figure S16). Also, $Mn/Ru-Co_3O_4$ exhibited minor charge transfer resistance (4 Ω) (Figure S17a) and Tafel slope (103 mV dec^{-1}) (Figure S17b), indicating the more efficient charge transfer process and faster reaction kinetics process. Electrochemical double layer capacitance (C_{dl}) calculated with CV test results showed $Mn/Ru-Co_3O_4$ had the largest C_{dl} of 103 mF cm^{-2}, indicating a much larger electrochemically active surface area (ECSA) (Figure S18).

ECSA was used to further normalized the geometric current density, which showed that the normalized current density of $Mn/Ru-Co_3O_4$ (9.5 μA cm^{-2}) is 13.5 × higher than Co_3O_4 (0.7 μA cm^{-2}) at 1.6 V vs. RHE (Figure S19). Considering both the activity and stability of acidic OER, the $Mn/Ru-Co_3O_4$ sample exhibited apparent advantages over other representative materials with such a low noble metal content (Fig. 4c, and Table S6).

Stability is another important factor in evaluating the electrocatalytic materials. As indicated by the result, Co_3O_4, $Mn-Co_3O_4$, and $Ru-Co_3O_4$ could only operate under 10 mA cm^{-2} for about 10 h in acidic media. However, the $Mn/Ru-Co_3O_4$ can operate for more than 120 h without noticeable degradation (Fig. 4d). The sample maintained good stability even under simulated practical operating conditions, such as electrolyte replacement, pause, restart actions and high current density (Figure S20).

Moreover, the Faradaic efficiency for all samples was nearly 100 %, indicating OER dominates the reaction process rather than the material corrosion (Figure S21). The crystal structure and components of $Mn/Ru-Co_3O_4$ were further investigated after stability testing, which demonstrated almost no change and further verified the stability of our acidic OER electrocatalysts (Figure S22 to S24, and Table S7). Furthermore, we also conducted the inductively coupled plasma optical emission spectroscopy (ICP-OES) to evaluate the leaching of Co, Mn, Ru during the OER process, which demonstrate that Mn/Ru co-doping significantly alleviated the leaching of the ions and enhance the stability of $Mn/Ru-Co_3O_4$. In contrast, Co_3O_4, $Mn-Co_3O_4$ and $Ru-Co_3O_4$ suffer from severe ions leaching during the stability test. These results proved that the co-doping effect would enhance the interatomic interactions, which is the main reason for the observed long-term stability in the acidic medium (Figure S25).

2.4. Mechanistic insights into the enhanced OER activities of $Mn/Ru-Co_3O_4$

For the acidic OER process, one of the most vital issues is the adsorption of *OH from deficient acidic environments. *In situ* EIS was then measured to track the OER process and detect the adsorption situation of different samples. *In situ* Bode phase plots of the four representative samples were demonstrated in Figure S26. There are two different peak regions in the *in situ* Bode plot, located at the middle-frequency region (between $10^0 \sim 10^1$ Hz) and the low-frequency region (below 10^0 Hz), which could be associated to the double-layer capacitance (DLC) induced by the accumulation of adsorbed intermediate (*OH), and the nonhomogeneous charge distributions caused by the OER process [46–48]. It showed clearly that for Co_3O_4 and $Mn-Co_3O_4$, no prominent peaks were observed, indicating the adsorption of *OH is not sufficient for the following OER step (Figure S26a and S26b). However, the $Ru-Co_3O_4$ and $Mn/Ru-Co_3O_4$ exhibit significant capacitive behavior, and the peaks belonging to DLC are more pronounced, suggesting a stronger *OH affinity, which would benefit the overall catalytic driving force.

Moreover, it can also be seen clearly that Ru doping and Mn/Ru doping would result in the low-frequency peak appearing earlier than Co_3O_4 and $Mn-Co_3O_4$, indicating these two materials were more accessible to be polarized to initiate the OER process even in the harsh acidic condition (Figure S26c and S26d). The *in situ* EIS measurements indicated that Ru dopant was an essential factor in enhancing the first adsorption step of *OH as well as increasing the active sites in the catalytic materials [49]. Moreover, Mn/Ru-co-doping will not only enhance the adsorption process but also reduce the polarization potential to activate the acidic OER process.

The subsequent deprotonation process of the adsorbed *OH is another essential step for OER. Methanol served as the molecular probe to investigate the surface *OH coverage on different samples; since methanol molecules were more prone to nucleophilic attack, the electrophilic *OH, the methanol oxidation reaction (MOR) was more active on *OH dominated surfaces [50]. MOR and OER were competing reactions for the same intermediate (*OH), so when methanol was added into the H_2SO_4 solution, both Co_3O_4 and $Mn-Co_3O_4$ demonstrated relatively high MOR activities, which proved the adsorbed *OH dominated the catalysts surface [51] (Figure S27a and S27b). However, when it comes to $Ru-Co_3O_4$ and $Mn/Ru-Co_3O_4$, the MOR activities were close to or even lower than the OER activities, which verified the adsorbed *OH could be easily deprotonated (Figure S27c and S27d). Combined with the previous *in situ* EIS results, it could be concluded that doping with Ru or Mn/Ru co-doping could enhance both reactant adsorption capability and deprotonation ability simultaneously, which could lower the energy barrier of the rate-determining-step (RDS) in the reaction.

Although both Ru-doped and Mn/Ru co-doped Co_3O_4 exhibited better intermediate adsorption capability and deprotonation ability than the undoped Co_3O_4, the acidic OER activities of these two samples were still different (η_{10} for $Ru-Co_3O_4$ and $Mn/Ru-Co_3O_4$ were 380 mV and 230 mV, respectively). This suggests that there might be some differences in the catalytic mechanisms for the two samples. Considering the theoretical limitation by a so-called scaling relation between the intermediates *OH and *OOH in the traditional AEM with the overpotential limit of 370 mV [14], there were compelling reasons to believe that when Mn and Ru were co-doped, the reaction pathway undergoes significant changes, enabling it to surpass the overpotential limit. Based on the above considerations, we further investigated the possible mechanism of acid OER mechanisms in different samples. Previous reports have proved that the OER activities of electrocatalysts with the LOM pathway would demonstrate strong pH dependence at the RHE scale due to the nonconcerted proton-electron transfer (NCPET) process [11,52]. Fig. 4e and 4f demonstrated the proton reaction orders on the RHE scale ($\rho^{RHE} = \partial logi/\partial pH$), obtained from the LSV curves at different pH solutions (Figure S28). The $Mn/Ru-Co_3O_4$ demonstrated the strongest pH dependence (ρ^{RHE} =-0.82) than other samples, which suggested the LOM dominated the OER process, while other samples (Co_3O_4, $Mn-Co_3O_4$ and $Ru-Co_3O_4$) would follow the AEM pathway.

To further validate the occurrence of LOM in $Mn/Ru-Co_3O_4$, we further performed *in situ* ^{18}O isotope labeling differential electrochemical mass spectrometry (DEMS) measurements. The $Mn/Ru-Co_3O_4$ was first labeled with ^{18}O isotopes, and then the evolved O_2 during OER was measured (See Methods section for more information). The DEMS measurement detected a strong mass signal of $m/z = 34$ and a relatively weak signal of $m/z = 36$ during the CV cycling process, indicating the presence of $^{16}O^{18}O$ ($^{34}O_2$) and $^{18}O_2$ ($^{36}O_2$) in the gas production (Fig. 4g). These results further proved that the activated lattice O atoms participated in the OER process. Moreover, the intensity of $^{16}O^{18}O$ is 10× higher than the $^{18}O_2$, further proving the LOM pathway would dominate the whole OER process, while another possible pathway involving the direct coupling of lattices O atoms (the so-called oxide path mechanism, OPM) will not dominate the reaction [13,53].

In situ Raman spectra were used to detect local structure variation. It could be seen that with the progress of the OER, there is a noticeable redshift in the position of the A_g peak, indicating that the O_V concentration in the Mn/Ru-Co_3O_4 gradually increased with the applied potential (Figure S29). The *in situ* and *ex situ* Raman results, combined with the EPR result, provide compelling evidence of a shift in the catalytic mechanism, which is closely associated with the presence of O_V.

Elemental doping was usually confided to be an efficient way to modify the OER reaction pathway [8,9,53]. However, the precise underlying mechanisms behind this phenomenon remain elusive. Even among closely related doping systems, conflicting reports are suggesting different OER mechanisms [9,13,54]. Considering the inherent randomness and uncertainty associated with doping strategies, the transition of the catalytic mechanism from AEM to LOM in the acidic OER process might be likely driven by deeper underlying factors rather than solely relying on elemental doping. In our experimental results, besides elemental doping, the main difference among the as-prepared samples lies in their distinct O_V concentrations, which showed an apparent correlation between catalytic performance and mechanism transition. Therefore, we have reason to speculate that the O_V in spinel oxides is the fundamental cause of the transition of the catalytic mechanism.

To corroborate the above hypothesis, we further designed experiments to validate the crucial role of vacancies in the transition of the catalytic mechanism. To eliminate the influence of elemental doping, we treated the Co_3O_4 NSs with $NaBH_4$ to create more O_V according to previous report [55,56]. It showed that after $NaBH_4$ treatment, the overpotential of Co_3O_4 obviously decreased ~ 10 % and ~ 28 % at the current density of 50 mA cm^{-2} and 100 mA cm^{-2}, respectively (Figure S30). Moreover, the acidic OER activities of $NaBH_4$ treated Co_3O_4 (Co_3O_4-O_V) also demonstrated relatively stronger pH dependence, indicating that O_V was the main reason for mechanism switching (Figure S31).

2.5. DFT calculations and the optimal reaction pathway

DFT calculations were conducted to provide insights into the reaction mechanism and reaction pathway of different samples. The previous characterization results demonstrated that Mn and Ru readily substitute the Co_{Oct} sites in the Co_3O_4 lattice, which was also verified by the DFT calculation results (Table S8). We assume Ru atoms as the most active catalytic sites [9,53], and considered two different Mn doping sites (A site and B site in Figure S32) to determine the final calculating models. The system exhibits more excellent stability at A site by 0.34 eV compared to B site, thus the model in Figure S32a was selected as the final calculation model for the co-doping Mn/Ru-Co_3O_4. Subsequently, we conducted calculations to evaluate the O_V formation energies of

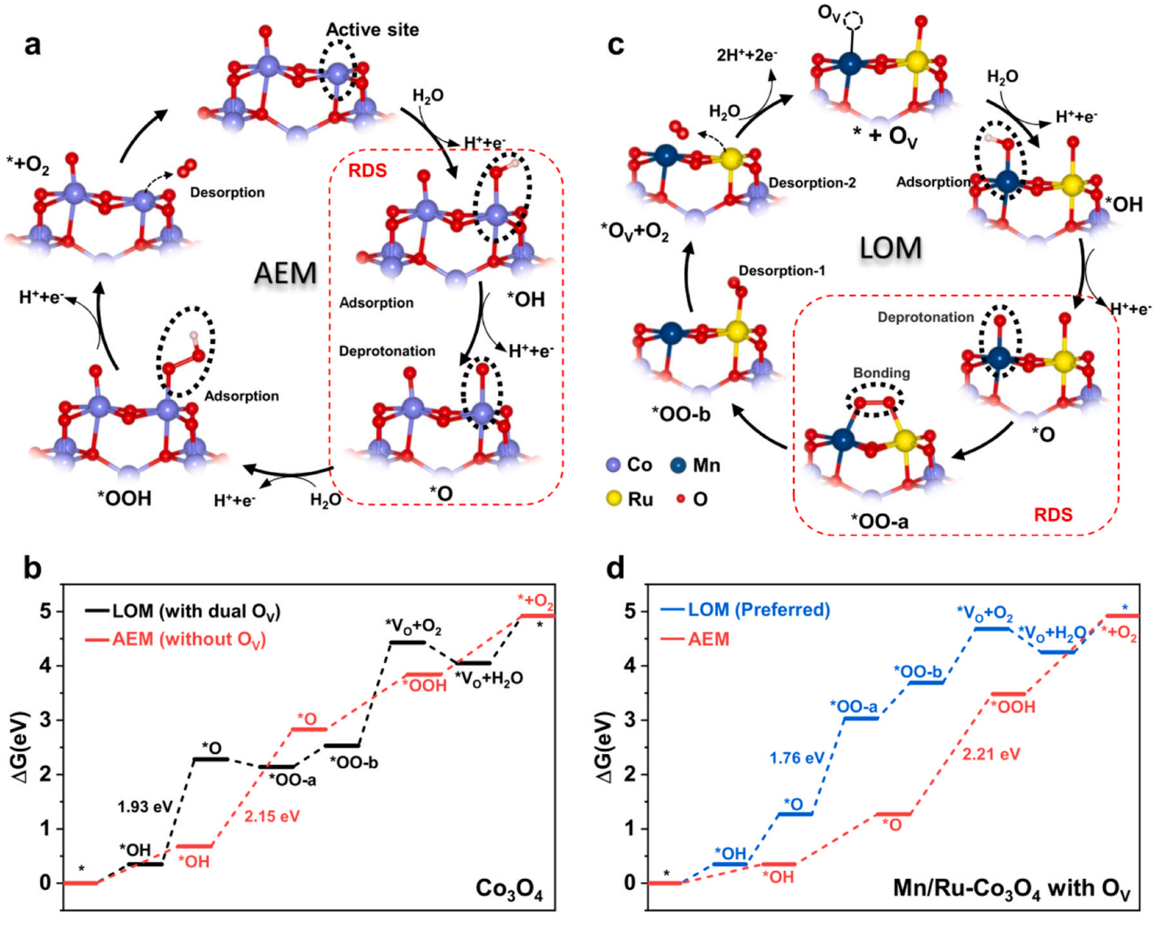

Fig. 5. OER mechanism analysis. a Schematic illustration of AEM on Co_3O_4 (113) surface and b the corresponding Gibbs free energy evolution via AEM. c Schematic illustration of LOM on Mn/Ru-Co_3O_4 (113) surface and the d corresponding Gibbs free energy evolution follow LOM and AEM, respectively. DFT calculation results demonstrated that co-doping inducing O_V would make the system tend to follow the LOM pathway with a lower energy barrier. Blue, cyan blue, yellow, and red represent Co, Mn, Ru, and O atoms, respectively.

Co_3O_4 and Mn/Ru-Co_3O_4. The results demonstrated that after Mn/Ru co-doping, the O_V formation energy increased from the initial −1.34 eV (Co_3O_4) to −0.48 eV (O_V around the Mn site in Mn/Ru-Co_3O_4) and 0.06 eV (O_V around the Mn site in Mn/Ru-Co_3O_4), indicating Mn/Ru co-doping could make the system more prone to generate vacancies than the Co_3O_4 (Figure S33), which consist with the EPR result in Fig. 3c.

According to the Gibbs free energy diagrams, the OER process on pristine Co_3O_4 proceeds exclusively via the AEM pathway without the involvement of lattice oxygen vacancies (Fig. 5a), which is consistent with previous reports [28,31]. The rate-determining step (RDS) for the AEM pathway on Co_3O_4 is identified as the deprotonation of the first *OH intermediate (*OH → *O), with an energy barrier of 2.15 eV (Fig. 5b). For the Mn/Ru co-doped Co_3O_4 models, oxygen vacancies were introduced at two representative positions around the Ru active site (Fig. 5c and Figure S34). Regardless of whether the oxygen vacancy is located adjacent to the Mn site or in the vicinity of Ru, the calculated Gibbs free energy profiles reveal a clear tendency for the OER to proceed via LOM pathway, since the energy barrier of RDS for AEM pathway is 2.21 eV, which is much higher than that for LOM pathway (1.76 eV). Notably, the corresponding energy barriers are significantly reduced from 2.15 eV to 1.76 and 1.77 eV, respectively, compared with that of pristine Co_3O_4 (Fig. 5d and Figure S34c).

Furthermore, the RDS for the Mn/Ru-Co_3O_4 models shifts to the oxygen-oxygen bond formation step, indicating a facilitated deprotonation process relative to Co_3O_4. This mechanistic evolution is consistent with the MOR results (Figure S27), further supporting the dominance of the LOM pathway upon co-doping and oxygen vacancy introduction.

To further investigate the origin of the catalytic reaction mechanism transition, we proceeded to exclude the influence of doping factors. We calculated the effects of different oxygen vacancy concentrations on the catalytic reaction mechanism of undoped Co_3O_4. Three representative configurations were considered, including two cases with a single oxygen vacancy located near the active site (Figures S35 and S36) and one case with dual oxygen vacancies in the vicinity of the active site (Figure S37). The calculation results show that when only a single oxygen vacancy is present, Co_3O_4 still preferentially follows the conventional AEM pathway, with the deprotonation step (*OH → *O) remaining the rate-determining step and energy barriers of 2.01 eV and 1.98 eV, respectively (Figures S35b and S36b). Notably, the persistence of the AEM pathway indicates that a single vacancy does not sufficiently weaken the metal-oxygen bonding or promote lattice oxygen oxidation, highlighting that isolated defects alone are insufficient to trigger the reaction pathway transition. The introduction of an oxygen vacancy results in a progressively increasing energy barrier for OOH generation. When introducing a dual Ov, this leads to the transition in the RDS for *OOH formation, a prerequisite for LOM. A lower reaction energy barrier of 1.93 eV is observed via LOM, compared to 2.15 eV for the pristine (113) facet via AEM (as shown in Fig. 5b and Figure S37). Considering the distinction between the undoped Co_3O_4 and Mn/Ru-Co_3O_4, as well as the previous results of the MOR reaction, it could be concluded that elemental doping, especially the doping of Ru atoms, is essential not only for providing active sites for the reaction but also for facilitating the deprotonation step, but the catalytic mechanism switch was mainly originated from the existence of O_V around the active sites.

2.6. Back-to-back experiments validating the O_V induced LOM mechanism

To further substantiate the universality of our hypothesis that O_V triggered the mechanism switch from AEM to LOM, we further expand the study to another typical spinel oxide Mn_3O_4 (Supplementary Note 1). The samples were also synthesized with electrodeposition methods (See Methods section for details). After a series of optimization selections, the deposition duration was standardized to 30 min, ensuring an equal loading of electrocatalysts across all samples (Figure S38-S40).

We designed two different groups of samples according to the presence or absence of Ru doping in Mn_3O_4 (Ru-Mn_3O_4, and Mn_3O_4). To generate O_V in Mn_3O_4, the samples were then treated with $NaBH_4$ solution, resulting in the formation of samples rich in O_V (Ru-Mn_3O_4-O_V and Mn_3O_4-O_V). PXRD patterns and the corresponding Raman spectra demonstrated typical characteristics of Mn_3O_4, suggesting the reduction process with $NaBH_4$ would not significantly influence the crystal structure (Figure S41 and S42). TEM images demonstrated no oblivious lattice distortion, which further proved the reduction process did not obviously disrupt the crystal structure of the material. EDS spectra of all samples showed that, after reduction with $NaBH_4$, the elements would remain close to their stoichiometric ratios, but there would be a slight decrease in oxygen content (Figure S43-S50, and Table S9). The representative Ru-Mn_3O_4-O_V sample was further characterized using atomic-resolution iDPC-STEM image and the corresponding EDS mapping, which revealed the uniform distribution of Ru in a single-atom state throughout the sample (Fig. 6a and 6b). EPR spectra also clearly showed that treatment with $NaBH_4$ would increase the concentration of O_V (Fig. 6c). Surface chemical states of all samples were also characterized with XPS. The results demonstrated that after the reduction process with $NaBH_4$ solution, the oxidation state of metal cations was reduced in Mn_3O_4-O_V and Ru-Mn_3O_4-O_V (Figure S51, S52 and Table S10). The concentration of O_V on the surface was significantly increased (Figure S53 and Table S11), which agrees well with the EPR results.

The acidic OER performances were measured in 0.5 M H_2SO_4. It showed that creating O_V, regardless of Ru doping, can significantly enhance catalytic activity. Moreover, Ru doping can further enhance catalytic activity. Specifically, creating O_V can reduce the η_{10} for Mn_3O_4 and Ru-Mn_3O_4 from 540 mV and 360 mV to 440 mV and 230 mV, respectively (Fig. 6d). The OER mechanisms were investigated by checking the pH dependence of various samples (Fig. 6e; Figure S54). Mn_3O_4-O_V and Ru-Mn_3O_4-O_V demonstrated strong pH dependence (ρ^{RHE} =-0.86 and −0.85, respectively), indicating the OER process on their surface followed the LOM pathway. In contrast, Mn_3O_4 and Ru-Mn_3O_4 showed relatively weak pH dependence (ρ^{RHE} =-0.22 and −0.32, respectively), and this proved that Ru doping is not the main reason for the OER mechanism switch from AEM to LOM.

DEMS spectrum was conducted to further prove the existence of the LOM pathway in the representative Ru-Mn_3O_4-O_V. Similar to the situation of Mn/Ru-Co_3O_4, the strong mass signal of $m/z = 34$ indeed proved the OER process on the O_V abundant surface would undergo the LOM pathway (Fig. 6f). It should be mentioned that the catalytic activities of Mn_3O_4-O_V were relatively lower than the Ru-Mn_3O_4, even though the LOM was dominant for Mn_3O_4-O_V. This indicates that while the change in mechanism can significantly promote the optimization of reaction steps and energy barriers, it still requires the presence of additional reactive sites to achieve the overall optimum catalytic activity of the catalyst. We further sintered the Mn_3O_4-O_V and Ru-Mn_3O_4-O_V at 300 ℃ for 2 h to partially replenish the O_V in the samples, abbreviated as Mn_3O_4-O_V-Anneal, and Ru-Mn_3O_4-O_V-Anneal (Figure S55). The OER activities were slightly decreased in the sintered samples, further confirming the significant role of O_V in modulating the intrinsic OER activities of spinel oxides (Figure S56).

3. Conclusion

In this study, we systematically investigated the vital roles of O_V and elemental doping for the acidic OER mechanism switch in spinal oxides. Theoretical and experimental results demonstrate that the transition of the catalytic mechanism in the spinel oxide system primarily originates from O_V near the active sites. Elements doping also showed an essential role in enhancing the catalytic activities of Mn/Ru-Co_3O_4, which primarily serves to stabilize the crystal structure, provide active sites, and optimize specific reaction steps. However, in terms of the intrinsic catalytic mechanism transition, doping does not play a decisive role in inducing the change. By synergistically regulating O_V, doping elements,

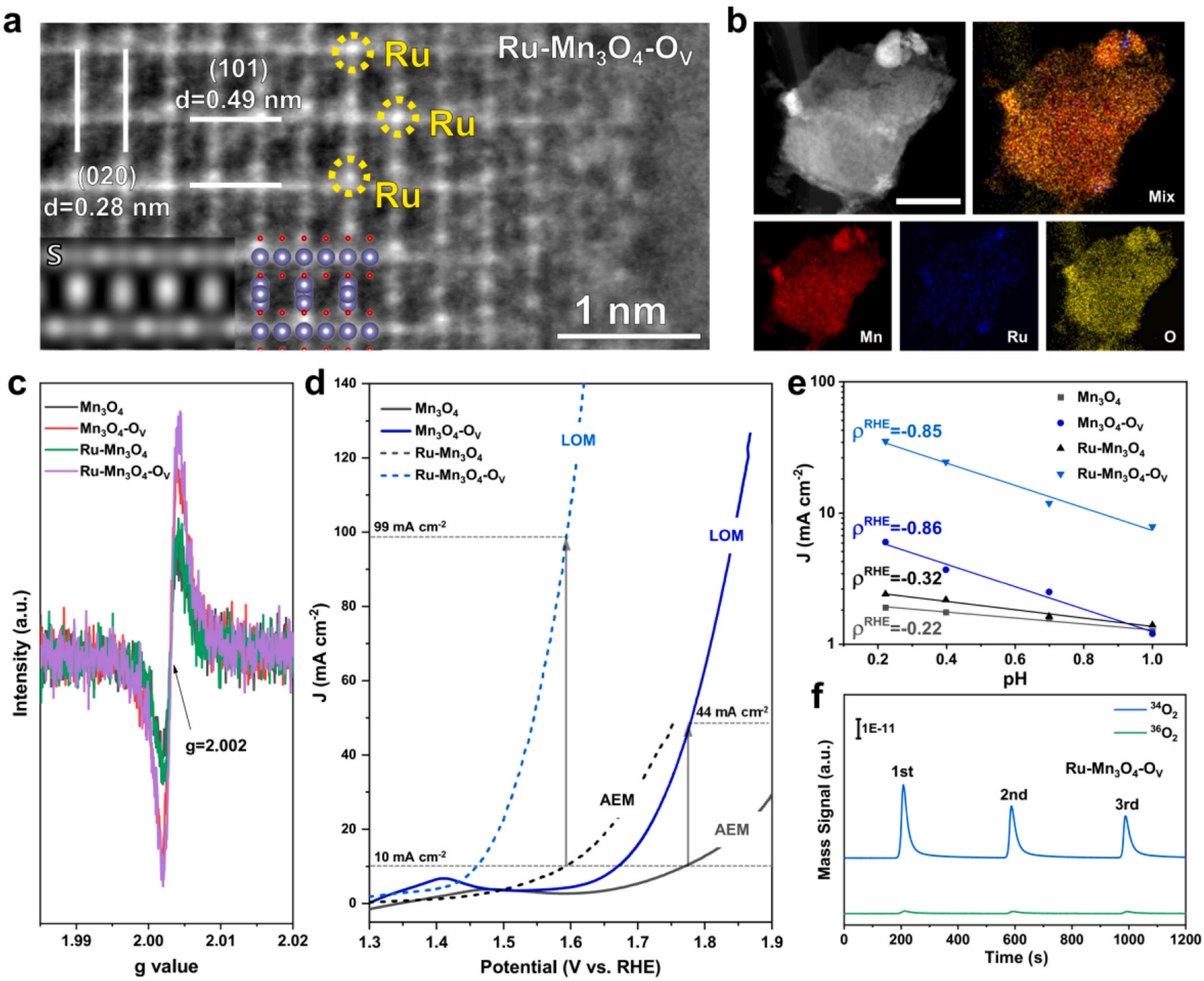

Fig. 6. Characterizations and electrochemical measurements for Mn_3O_4 based spinel oxides. a iDPC-STEM image of Ru-Mn_3O_4-O_V along [$\bar{1}$01] zone axis. Inset was the simulation image (labeled with "S") and the crystal structure image alone [$\bar{1}$01] zone axis. b The HAADF-STEM image and the corresponding EDS mapping of Ru-Mn_3O_4-O_V NSs (Scale bar: 50 nm). c EPR signal of O_V in Mn_3O_4, Mn_3O_4-O_V, Ru-Mn_3O_4-O_V and Ru-Mn_3O_4. d Acidic OER activities of different samples. e Current densities and the ρ^{RHE} of each sample obtained at 1.60 V vs. RHE plotted in log scale as a function of pH. f DEMS measurements of ^{34}O and ^{36}O signals from the reaction products for ^{18}O-labeled Ru-Mn_3O_4-O_V in 0.5 M H_2SO_4 in $H_2^{16}O$.

and their proportions, the acidic OER activity of Mn/Ru-Co_3O_4 was significantly improved 48 % (η_{10}=230 mV) compared with the undoped Co_3O_4 (η_{10}=440 mV) with low Ru doping (2.9 at%), and the stability was enhanced to about 120 h in 0.5 M H_2SO_4 media. Furthermore, the strategy of vacancy-induced acidic OER mechanism transition was also confirmed in another spinel oxide system, Mn_3O_4, which demonstrated its universality. Our results illustrate a route that can boost acidic OER activities in spinel oxides without the significant consumption of noble metals via synergistically modifying the coordination environment of active sites and defect structures.

4. Experimental section

4.1. Materials

All of the chemicals and materials were purchased from Aladdin Biochemical Technology Co., Ltd. in Shanghai, China, without further purification. The carbon cloth (HCP 331 N) substrate was obtained from Shanghai Hesen Electric Co., Ltd. Before use, the carbon cloth (CC) was ultrasonically cleaned for 30 min with acetone, deionized water, and ethanol, respectively, to remove any residual surface contaminants.

4.2. Synthesis of Co_3O_4, Mn-Co_3O_4, Ru-Co_3O_4, and Mn/Ru-Co_3O_4

The corresponding studied electrocatalysts were directly prepared on CC with the electrodeposition method. $Co(NO_3)_2{\cdot}6H_2O$, $Mn(NO_3)_2{\cdot}4H_2O$, and $RuCl_3$ were used to serve as sources of Co, Mn, and Ru, respectively. After a series of optimizations, we have ultimately chosen a concentration of 25 mM for Co ions in the electrolyte solution. The doped Mn and Ru contents are controlled at 4 mg mL^{-1}. For the electrodeposition of Mn/Ru-Co_3O_4, a piece of cleaned CC (2 cm × 2 cm), an Ag/AgCl electrode, and Pt wire was used to serve as the working electrode, reference electrode, and counter electrode. The deposition was carried out under a constant current of 40 mA (i.e., a current density of 10 mA cm^{-2}), and the deposition time was 30 min. After that, the CC was thoroughly rinsed with deionized water and ethanol and dried at 60 ℃ for 8 h for further use. After the drying process was completed, the sample was sintered in air for 2 h at 350 ℃, and the Mn/Ru-Co_3O_4 was obtained. The preparation of Co_3O_4, Mn-Co_3O_4 and Ru-Co_3O_4 were similar to Mn/Ru-Co_3O_4, except the reduction of the corresponding dopant component. Co_3O_4-O_V was prepared by immersing Co_3O_4 in a $NaBH_4$ solution (0.1 M) for 30 min, and then thoroughly rinsed with deionized water. The final loading amount of the electrocatalysts was about 1.5 mg cm^{-2}

4.3. Synthesis of Mn_3O_4, Mn_3O_4-O_V, Ru-Mn_3O_4, and Ru-Mn_3O_4-O

Mn_3O_4, Mn_3O_4-O_V, Ru-Mn_3O_4, and Ru-Mn_3O_4-O_V are also prepared with the electrodeposition method. Typically, Mn_3O_4 was prepared on a piece of CC (2 cm× 2 cm) using a 50 mM $Mn(NO_3)_2$ solution as the electrolyte. The deposition was also carried out under a constant current of 40 mA (i.e., a current density of 10 mA cm^{-2}), and the deposition time was 30 min. After drying for 8 h, the sample was sintered in air for 2 h at 350 ℃, and the Mn_3O_4 was obtained. In order to further reduce the influence of Ru on the determination of reaction mechanisms, the concentration of Ru ion in the electrolyte was further reduced to 1 mg mL^{-1}. The preparation of Ru-Mn_3O_4 was carried out using a similar procedure as that of Mn_3O_4. To create oxygen vacancies, the prepared Mn_3O_4 and Ru-Mn_3O_4 were immersed in a $NaBH_4$ solution (0.1 M) for 30 min, and then thoroughly rinsed with deionized water. The final productions were Mn_3O_4-O_V and Ru-Mn_3O_4-O_V, respectively.

4.4. Characterizations

XRD patterns were conducted by a Rigaku SmartLab 9 kW X-ray diffractometer with Cu Kα radiation ($\lambda = 1.5418$ Å). The transmission electron microscope (JEOL, JEM-2100F; acceleration voltage, 200 kV), and double spherical aberration-corrected transmission electron microscope (Thermo Fisher Spectra 300, operated at 300 kV) were employed to investigate the morphologies, microstructures, and elements distribution. Dr. Probe was used for simulating STEM-HAADF images. Accelerating voltage, convergence semi-angle, and collection angle were set the same as the imaging, which was 300 kV, 15 mrad, and 35–200 mrad, respectively. Raman spectroscopy was conducted on a WITec, alpha300 R equipment (with a 532 nm laser). EPR spectra were obtained on a Bruker A300–10–12 spectrometer. The XANES and EXAFS measurements were carried out at the XAFCA beamline of the Singapore Synchrotron Light Source (SSLS) and BL01B01 beamline at the SPring-8 at Japan Synchrotron Radiation Research Institute (JASRI). The XAS data were analyzed using the Demeter package [57].

4.5. Electrochemical measurements

All electrochemical measurements in this project were conducted on a CHI 760E electrochemical workstation (CH Instruments, Inc. Shanghai) using a typical three-electrode cell. The as-systemized self-standing electrodes, Ag/AgCl electrode, and a graphite rod were used as the working electrode, reference electrode, and counter electrode, respectively. O_2-saturated 0.5 M H_2SO_4 solution was used to serve as an electrolyte at room temperature. Before the LSV test, all working electrodes were activated by the cyclic voltammetry (CV) technique for 100 cycles to obtain stable LSV curves. LSV curves were then obtained with a scan rate of 2 mV s^{-1}. In this work, all potentials were converted to RHE with the equation $E_{RHE}=E_{Ag/AgCl} + 0.197\ V + 0.059 \times pH$. EIS measurements were carried out within a frequency range of 10^6 Hz to 10^{-2} Hz, and the charge transfer resistance (R_{ct}) obtained by fitting the EIS data was used for the *iR* correction. The stability test was also conducted in 0.5 M H_2SO_4, with the prepared samples serving as the wording electrode, and Ag/AgCl electrode, and a graphite rod serving as the reference electrode, and counter electrode, respectively. Meanwhile, during the stability test, we replaced the electrolyte at the 65 h and randomly paused for two hours at the 95 h and 110 h to simulate the stability of the electrode under actual working conditions.

4.6. Differential electrochemical mass spectrometric measurements (DEMS)

The *in situ* DEMS experiments were performed with an *in situ* differential electrochemical mass spectrometer provided by Linglu Instruments (Shanghai) Co. Ltd. The experiment is divided into two main steps. The first step is labeling the sample with ^{18}O isotope in ^{18}O-labelled 0.5 M H_2SO_4 solution with CV cycling (scan rate 10 mV s^{-1}, potential range 1.0–1.6 V vs. Ag/AgCl). After that, the resultant electrodes were thoroughly rinsed with deionized water ($H_2^{16}O$) for several times to remove the residual $H_2^{18}O$. The second step is the DEMS measurement. In this process, the potential of the CV range was also fixed at 1.0 – 1.6 V vs. Ag/AgCl, with a scan rate of 10 mV s^{-1}. In the meantime, gas products of different molecular weights generated during the OER process were measured in real time by mass spectroscopy.

4.7. DFT calculations

To examine the structural configurations and electronic characteristics of Mn- and Ru-doped Co_3O_4 materials, spin-polarized DFT calculations were carried out employing the Vienna ab initio Simulation Package (VASP) software [58,59] suite with the projector augmented wave (PAW) [60]. The exchange-correlation interactions were described using the Perdew, Burke, and Ernzernhof (PBE) functional [61] with the generalized gradient approximation (GGA) [62]. The kinetic energy cutoff for the plane-wave basis set was established at 450 eV, and a vacuum layer of more than 20 Å was implemented to avoid interlayer interactions. To account for van der Waals interactions on the surface, the DFT-D3 scheme developed by Grimme was applied [63]. The electronic self-consistent field (SCF) convergence criterion was set to 10^{-4} eV. Fully relaxed geometries were achieved by optimizing all atomic positions until the forces reached a magnitude of less than 0.05 eV/Å. The structural optimizations were carried out using a gamma-centered Monkhorst-Pack k-point sampling scheme [64] with k-point samplings of $3 \times 3 \times 1$. In our study on the thermodynamic stability of Co_3O_4, we utilized the GGA+U method to account for the significant localization of *d*-electrons. Specifically, we applied a Hubbard U value of 4.8 eV for Mn D-states [65], 6.7 eV for Ru [66], and 2.8 eV for Co [67]. The corrections to the Gibbs free energies originate from the calculated zero-point energy on Ru sites of doped Co_3O_4 and the entropic (TS) contribution, with similar adjustments approximated for Mn and Co. The corrections for OH, O, and OOH are 0.35, 0.05, and 0.35 eV at standard conditions (298.15 K, 1 atm), respectively. The adjustments for H_2 and H_2O are obtained from the National Institute of Standards and Technology (NIST).

CRediT authorship contribution statement

Wenqian Shen: Data curation. **Tao Ling:** Investigation. **Chi Shing Tsang:** Data curation. **Honglin Chen:** Data curation. **Thuc Hue Ly:** Supervision, Methodology, Investigation, Funding acquisition. **Qingming Deng:** Writing – review & editing, Supervision, Project administration, Investigation, Funding acquisition, Formal analysis, Data curation, Conceptualization. **Jiong Zhao:** Writing – review & editing, Supervision, Resources, Project administration, Funding acquisition, Conceptualization. **Lok Wing Wong:** Data curation. **Xiaodong Zheng:** Data curation. **Qiang Fu:** Writing – original draft, Methodology, Investigation, Formal analysis, Data curation, Conceptualization.

Declaration of Competing Interest

The authors declare that they have no known competing financial interests or personal relationships that could have appeared to influence the work reported in this paper.

Acknowledgements

This work was supported by the National Science Foundation of China (Project No. 52173230, 52222218, 52402003, 52272045, 52525308), The Hong Kong Research Grant Council (Project No. 11312022, 15302522, C5067-23G), City University of Hong Kong (Project No. 7005602, 9229074, 9667223), The Innovation and Technology Fund (project no. ITS/014/23), The State Key Laboratory of Marine Pollution (SKLMP) Seed Collaborative Research Fund SKLMP/SCRF/0037, The Hong Kong Polytechnic University (Project No. SAC9), the Research Institute for Advanced Manufacturing of The Hong Kong Polytechnic University, Shenzhen Science, Technology and Innovation Commission (Project No. SGDX20230821092059005), Natural Science Foundation of Jiangsu Province of China (Project No. BK20211609). The Postdoctoral Fellowship Program of CPSF (Project No. GZC20242200). The China Postdoctoral Science Foundation (Project No. 2024M764162).

Appendix A. Supporting information

Supplementary data associated with this article can be found in the online version at doi:10.1016/j.nanoen.2026.111731.

Data availability

Data will be made available on request.

References

[1] L.C. Seitz, C.F. Dickens, K. Nishio, Y. Hikita, J. Montoya, A. Doyle, C. Kirk, A. Vojvodic, H.Y. Hwang, J.K. Norskov, A highly active and stable IrO x/$SrIrO_3$ catalyst for the oxygen evolution reaction, Science 353 (2016) 1011–1014, https://doi.org/10.1126/science.aaf5050.

[2] A. Li, S. Kong, C. Guo, H. Ooka, K. Adachi, D. Hashizume, Q. Jiang, H. Han, J. Xiao, R. Nakamura, Enhancing the stability of cobalt spinel oxide towards sustainable oxygen evolution in acid, Nat. Catal. 5 (2022) 109–118, https://doi.org/10.1038/s41929-021-00732-9.

[3] C. Hu, K. Yue, J. Han, X. Liu, L. Liu, Q. Liu, Q. Kong, C.-W. Pao, Z. Hu, K. Suenaga, Misoriented high-entropy iridium ruthenium oxide for acidic water splitting, Sci. Adv. 9 (2023) eadf9144, https://doi.org/10.1126/sciadv.adf9144.

[4] L. An, C. Wei, M. Lu, H. Liu, Y. Chen, G.G. Scherer, A.C. Fisher, P. Xi, Z.J. Xu, C. H. Yan, Recent development of oxygen evolution electrocatalysts in acidic environment, Adv. Mater. 33 (2021) 2006328.

[5] X. Li, X. Guan, L. Zhu, H. Li, X. Yin, S. Sun, H. Xu, Y. Fan, P. Li, L. Hu, Z. Wu, H. Pan, X. Wang, Z. Cheng, B. Jia, T. Ma, Electron transfer in catalysis: from fundamentals to strategies, Chem. Soc. Rev. 54 (2025) 11423–11467, https://doi.org/10.1039/D4CS00600C.

[6] S. Hao, H. Sheng, M. Liu, J. Huang, G. Zheng, F. Zhang, X. Liu, Z. Su, J. Hu, Y. Qian, Torsion strained iridium oxide for efficient acidic water oxidation in proton exchange membrane electrolyzers, Nat. Nanotechnol. 16 (2021) 1371–1377, https://doi.org/10.1038/s41565-021-00986-1.

[7] J. Yu, F.A. Garcés-Pineda, J. González-Cobos, M. Peña-Díaz, C. Rogero, S. Giménez, M.C. Spadaro, J. Arbiol, S. Barja, J.R. Galán-Mascarós, Sustainable oxygen evolution electrocatalysis in aqueous 1 M H_2SO_4 with earth abundant nanostructured Co_3O_4, Nat. Commun. 13 (2022) 4341, https://doi.org/10.1038/s41467-022-32024-6.

[8] L. Chong, G. Gao, J. Wen, H. Li, H. Xu, Z. Green, J.D. Sugar, A.J. Kropf, W. Xu, X.-M. Lin, La-and Mn-doped cobalt spinel oxygen evolution catalyst for proton exchange membrane electrolysis, Science 380 (2023) 609–616, https://doi.org/10.1126/science.ade1499.

[9] Y. Wang, Y.-P. Qin, S.-J. Liu, Y.-Z. Zhao, L. Liu, D. Zhang, S.-Q. Zhao, J.-F. Liu, Y.-D. Liu, H.-Y. Wu, B.-R. Jia, X.-H. Qu, H. Li, M.-L. Qin, Mesoporous single-crystalline particles as robust and efficient acidic oxygen evolution catalysts, J. Am. Chem. Soc. 16 (2025) 13345–13355, https://doi.org/10.1021/jacs.4c18390.

[10] Z.-M. Wei, Y.-X. Ding, W.-L. Shi, F.-Y. Zhang, Y.-X. Song, X. Cui, Y. Guo, L.-C. Sun, Q.-L. Jiang, B.-B. Zhang, Lanthanum-assisted lattice anchoring of iridium in Co_3O_4 for efficient oxygen evolution reaction in low-iridium water electrolysis, Nat. Commun. 16 (2025) 8145, https://doi.org/10.1038/s41467-025-63577-x.

[11] A. Grimaud, O. Diaz-Morales, B. Han, W.T. Hong, Y.-L. Lee, L. Giordano, K. A. Stoerzinger, M.T. Koper, Y. Shao-Horn, Activating lattice oxygen redox reactions in metal oxides to catalyse oxygen evolution, Nat. Chem. 9 (2017) 457–465, https://doi.org/10.1038/nchem.2695.

[12] Z.-F. Huang, J. Song, Y. Du, S. Xi, S. Dou, J.M.V. Nsanzimana, C. Wang, Z.J. Xu, X. Wang, Chemical and structural origin of lattice oxygen oxidation in Co–Zn oxyhydroxide oxygen evolution electrocatalysts, Nat. Energy 4 (2019) 329–338, https://doi.org/10.1038/s41560-019-0355-9.

[13] N. Wang, P. Ou, R.K. Miao, Y. Chang, Z. Wang, S.-F. Hung, J. Abed, A. Ozden, H.-Y. Chen, H.-L. Wu, Doping shortens the metal/metal distance and promotes OH coverage in non-noble acidic oxygen evolution reaction catalysts, J. Am. Chem. Soc. 145 (2023) 7829–7836, https://doi.org/10.1021/jacs.2c12431.

[14] I.C. Man, H.Y. Su, F. Calle-Vallejo, H.A. Hansen, J.I. Martínez, N.G. Inoglu, J. Kitchin, T.F. Jaramillo, J.K. Nørskov, J. Rossmeisl, Universality in oxygen evolution electrocatalysis on oxide surfaces, ChemCatChem 3 (2011) 1159–1165, https://doi.org/10.1002/cctc.201000397.

[15] G. Li, A. Priyadarsini, Z. Xie, S. Kang, Y. Liu, X. Chen, S. Kattel, J. Chen, Achieving higher activity of acidic oxygen evolution reaction using an atomically thin layer of IrO_x over Co_3O_4, J. Am. Chem. Soc. 147 (2025) 7008–7016, https://doi.org/10.1021/jacs.4c17915.

[16] C. Rong, H. Zhuang, Q. He, Q. Sun, S. Wu, J. Chen, Z. Han, C. Zhao, Uncoordinated single-site Ru confined in spinel Co_3O_4 lattice for high-performance and low-cost PEM water electrolysis, Adv. Funct. Mater. (2025) e16742, https://doi.org/10.1002/adfm.202516742".

[17] Z. Shi, Y. Wang, J. Li, X. Wang, Y. Wang, Y. Li, W. Xu, Z. Jiang, C. Liu, W. Xing, Confined Ir single sites with triggered lattice oxygen redox: toward boosted and sustained water oxidation catalysis, Joule 5 (2021) 2164–2176, https://doi.org/10.1016/j.joule.2021.05.018.

[18] Z. Wei, Y. Ding, W. Shi, F. Zhang, Y. Song, X. Cui, Y. Guo, L. sun, Q. Jiang, B. Zhang, Lanthanum-assisted lattice anchoring of iridium in Co_3O_4 for efficient oxygen evolution reaction in low-iridium water electrolysis, Nat. Commun. 16 (2025) 8145, https://doi.org/10.1038/s41467-025-63577-x.

[19] Y. Pan, X. Xu, Y. Zhong, L. Ge, Y. Chen, J.-P.M. Veder, D. Guan, R. O'Hayre, M. Li, G. Wang, Direct evidence of boosted oxygen evolution over perovskite by enhanced lattice oxygen participation, Nat. Commun. 11 (2020) 2002, https://doi.org/10.1038/s41467-020-15873-x.

[20] L. Li, P. Wang, Q. Shao, X. Huang, Recent progress in advanced electrocatalyst design for acidic oxygen evolution reaction, Adv. Mater. 33 (2021) 2004243, https://doi.org/10.1002/adma.202004243.

[21] J. Shan, Y. Zheng, B. Shi, K. Davey, S.-Z. Qiao, Regulating electrocatalysts via surface and interface engineering for acidic water electrooxidation, ACS Energy Lett. 4 (2019) 2719–2730, https://doi.org/10.1021/acsenergylett.9b01758.

[22] M. Huynh, D.K. Bediako, D.G. Nocera, A functionally stable manganese oxide oxygen evolution catalyst in acid, J. Am. Chem. Soc. 136 (2014) 6002–6010, https://doi.org/10.1021/ja413147e.

[23] C. Lin, J.-L. Li, X. Li, S. Yang, W. Luo, Y. Zhang, S.-H. Kim, D.-H. Kim, S.S. Shinde, Y.-F. Li, Z.-P. Liu, Z. Jiang, J.-H. Lee, In-situ reconstructed Ru atom array on α-MnO_2 with enhanced performance for acidic water oxidation, Nat. Catal. 4 (2021) 1012–1023, https://doi.org/10.1038/s41929-021-00703-0.

[24] A. Li, H. Ooka, N. Bonnet, T. Hayashi, Y. Sun, Q. Jiang, C. Li, H. Han, R. Nakamura, Stable potential windows for long-term electrocatalysis by manganese oxides under acidic conditions, Angew. Chem. Int. Ed. 131 (2019) 5108–5112, https://doi.org/10.1002/anie.201813361.

[25] J. Peng, L. Giordano, T.C. Davenport, Y. Shao-Horn, Stability design principles of manganese-based oxides in acid, Chem. Mater. 34 (2022) 7774–7787, https://doi.org/10.1021/acs.chemmater.2c01233.

[26] M. Huynh, C. Shi, S.J. Billinge, D.G. Nocera, Nature of activated manganese oxide for oxygen evolution, J. Am. Chem. Soc. 137 (2015) 14887–14904, https://doi.org/10.1021/jacs.5b06382.

[27] D.S. Raja, P.-Y. Cheng, C.-C. Cheng, S.-Q. Chang, C.-L. Huang, S.-Y. Lu, In-situ grown metal-organic framework-derived carbon-coated Fe-doped cobalt oxide nanocomposite on fluorine-doped tin oxide glass for acidic oxygen evolution reaction, Appl. Catal. B 303 (2022) 120899, https://doi.org/10.1016/j.apcatb.2021.120899.

[28] J. Huang, H. Sheng, R.D. Ross, J. Han, X. Wang, B. Song, S. Jin, Modifying redox properties and local bonding of Co_3O_4 by CeO_2 enhances oxygen evolution catalysis in acid, Nat. Commun. 12 (2021) 3036, https://doi.org/10.1038/s41467-021-23390-8.

[29] S. Niu, X.-P. Kong, S. Li, Y. Zhang, J. Wu, W. Zhao, P. Xu, Low Ru loading RuO_2/(Co, $Mn)_3O_4$ nanocomposite with modulated electronic structure for efficient oxygen evolution reaction in acid, Appl. Catal. B 297 (2021) 120442, https://doi.org/10.1016/j.apcatb.2021.120442.

[30] N. Zhang, X. Feng, D. Rao, X. Deng, L. Cai, B. Qiu, R. Long, Y. Xiong, Y. Lu, Y. Chai, Lattice oxygen activation enabled by high-valence metal sites for enhanced water oxidation, Nat. Commun. 11 (2020) 4066, https://doi.org/10.1038/s41467-020-17934-7.

[31] Y. Zhu, J. Wang, T. Koketsu, M. Kroschel, J.-M. Chen, S.-Y. Hsu, G. Henkelman, Z. Hu, P. Strasser, J. Ma, Iridium single atoms incorporated in Co_3O_4 efficiently catalyze the oxygen evolution in acidic conditions, Nat. Commun. 13 (2022) 7754, https://doi.org/10.1038/s41467-022-35426-8.

[32] F.T. Haase, A. Rabe, F.-P. Schmidt, A. Herzog, H.S. Jeon, W. Frandsen, P. V. Narangoda, I. Spanos, K. Friedel Ortega, J. Timoshenko, T. Lunkenbein, M. Behrens, A. Bergmann, R. Schlögl, B. Roldan Cuenya, Role of nanoscale inhomogeneities in Co_2FeO_4 catalysts during the oxygen evolution reaction, J. Am. Chem. Soc. 144 (2022) 12007–12019, https://doi.org/10.1021/jacs.2c00850.

[33] Y. Chen, J.K. Seo, Y. Sun, T.A. Wynn, M. Olguin, M. Zhang, J. Wang, S. Xi, Y. Du, K. Yuan, W. Chen, A.C. Fisher, M. Wang, Z. Feng, J. Gracia, L. Huang, S. Du, H.-J. Gao, Y.S. Meng, Z.J. Xu, Enhanced oxygen evolution over dual corner-shared cobalt tetrahedra, Nat. Commun. 13 (2022) 5510, https://doi.org/10.1038/s41467-022-33000-w.

[34] J. Baek, M.D. Hossain, P. Mukherjee, J. Lee, K.T. Winther, J. Leem, Y. Jiang, W. C. Chueh, M. Bajdich, X. Zheng, Synergistic effects of mixing and strain in high entropy spinel oxides for oxygen evolution reaction, Nat. Commun. 14 (2023) 5936, https://doi.org/10.1038/s41467-023-41359-7.

[35] C.-W. Tung, Y.-Y. Hsu, Y.-P. Shen, Y. Zheng, T.-S. Chan, H.-S. Sheu, Y.-C. Cheng, H. M. Chen, Reversible adapting layer produces robust single-crystal electrocatalyst for oxygen evolution, Nat. Commun. 6 (2015) 8106, https://doi.org/10.1038/ncomms9106.

[36] F. Lin, I.M. Markus, D. Nordlund, T.-C. Weng, M.D. Asta, H.L. Xin, M.M. Doeff, Surface reconstruction and chemical evolution of stoichiometric layered cathode materials for lithium-ion batteries, Nat. Commun. 5 (2014) 3529, https://doi.org/10.1038/ncomms4529.

[37] L. Su, E. Jo, A. Manthiram, Protection of cobalt-free $LiNiO_2$ from degradation with localized saturated electrolytes in lithium-metal batteries, ACS Energy Lett. 7 (2022) 2165–2172, https://doi.org/10.1021/acsenergylett.2c01081.

[38] M. Li, C. Qiu, S. Dogel, P. Chen, D.D. Perovic, J.Y. Howe, Microstructure-dependent thermal stability of super-tetragonal nanocomposite films through in situ TEM/EELS study, ACS Appl. Mater. Interfaces 14 (2022) 52316–52323, https://doi.org/10.1021/acsami.2c16084.

[39] C.-Y. Yang, H. Zhang, W.-L. Zhou, Y.-H. Zhang, J.-L. Wu, X.-P. Qin, C.-R. Leng, X.-X. Zhang, J. Zhang, B.-J. Li, s He, Q.-H. Liu, Precise substitution of octahedral sites in compression-strained Co_3O_4 nanorods for enhanced acidic oxygen evolution, Nano Energy 141 (2025) 111143, https://doi.org/10.1016/j.nanoen.2025.111143.

[40] R. Zhang, L. Pan, B. Guo, Z.-F. Huang, Z. Chen, L. Wang, X. Zhang, Z. Guo, W. Xu, K.P. Loh, J.-J. Zou, Tracking the role of defect types in Co_3O_4 structural evolution and active motifs during oxygen evolution reaction, J. Am. Chem. Soc. 145 (2023) 2271–2281, https://doi.org/10.1021/jacs.2c10515.

[41] J. Bae, D. Shin, H. Jeong, C. Choe, Y. Choi, J.W. Han, H. Lee, Facet-dependent Mn doping on shaped Co_3O_4 crystals for catalytic oxidation, ACS Catal. 11 (2021) 11066–11074, https://doi.org/10.1021/acscatal.1c01666.

[42] Y. Qiao, S. Guo, K. Zhu, P. Liu, X. Li, K. Jiang, C.-J. Sun, M. Chen, H. Zhou, Reversible anionic redox activity in Na_3RuO_4 cathodes: a prototype Na-rich layered oxide, Energy Environ. Sci. 11 (2018) 299–305, https://doi.org/10.1039/C7EE03554C.

[43] S. Pan, H. Li, D. Liu, R. Huang, X. Pan, D. Ren, J. Li, M. Shakouri, Q. Zhang, M. Wang, C. Wei, L. Mai, B. Zhang, Y. Zhao, Z. Wang, M. Graetzel, X. Zhang, Efficient and stable noble-metal-free catalyst for acidic water oxidation, Nat. Commun. 13 (2022) 2294, https://doi.org/10.1038/s41467-022-30064-6.

[44] Y. Lin, Z. Tian, L. Zhang, J. Ma, Z. Jiang, B.J. Deibert, R. Ge, L. Chen, Chromium-ruthenium oxide solid solution electrocatalyst for highly efficient oxygen evolution reaction in acidic media, Nat. Commun. 10 (2019) 162, https://doi.org/10.1038/s41467-018-08144-3.

[45] Z.-F. Huang, S. Xi, J. Song, S. Dou, X. Li, Y. Du, C. Diao, Z.J. Xu, X. Wang, Tuning of lattice oxygen reactivity and scaling relation to construct better oxygen evolution electrocatalyst, Nat. Commun. 12 (2021) 3992, https://doi.org/10.1038/s41467-021-24182-w.

[46] H.-Y. Wang, S.-F. Hung, H.-Y. Chen, T.-S. Chan, H.M. Chen, B. Liu, In operando identification of geometrical-site-dependent water oxidation activity of spinel Co_3O_4, J. Am. Chem. Soc. 138 (2016) 36–39, https://doi.org/10.1021/jacs.5b10525.

[47] Y. Gan, Y. Ye, X. Dai, X. Yin, Y. Cao, R. Cai, B. Feng, Q. Wang, X. Zhang, La and S co-doping induced the synergism of multiphase nickel-iron nanosheets with rich oxygen vacancies to trigger large-current-density oxygen evolution and urea oxidation reactions, Small (2023) 2303250, https://doi.org/10.1002/smll.202303250.

[48] L. Zeng, W. Chen, Q. Zhang, S. Xu, W. Zhang, F. Lv, Q. Huang, S. Wang, K. Yin, M. Li, $CoSe_2$ subnanometer belts with Se vacancies and Ni substitutions for the efficient electrosynthesis of high-value-added nitriles coupled with hydrogen generation, ACS Catal. 12 (2022) 11391–11401, https://doi.org/10.1021/acscatal.2c02489.

[49] N. Zhang, Y. Hu, L. An, Q. Li, J. Yin, J. Li, R. Yang, M. Lu, S. Zhang, P. Xi, Surface activation and Ni-S stabilization in NiO/NiS_2 for efficient oxygen evolution reaction, Angew. Chem. Int. Ed. 61 (2022) e202207217, https://doi.org/10.1002/anie.202207217.

[50] Y. Wen, C. Liu, R. Huang, H. Zhang, X. Li, F.P. García de Arquer, Z. Liu, Y. Li, B. Zhang, Introducing Brønsted acid sites to accelerate the bridging-oxygen-assisted deprotonation in acidic water oxidation, Nat. Commun. 13 (2022) 4871, https://doi.org/10.1038/s41467-022-32581-w.

[51] H.B. Tao, Y. Xu, X. Huang, J. Chen, L. Pei, J. Zhang, J.G. Chen, B. Liu, A general method to probe oxygen evolution intermediates at operating conditions, Joule 3 (2019) 1498–1509, https://doi.org/10.1016/j.joule.2019.03.012.

[52] L. Giordano, B. Han, M. Risch, W.T. Hong, R.R. Rao, K.A. Stoerzinger, Y. Shao-Horn, pH dependence of OER activity of oxides: current and future perspectives, Catal. Today 262 (2016) 2–10, https://doi.org/10.1016/j.cattod.2015.10.006.

[53] W. Zhu, F. Yao, K. Cheng, M. Zhao, C.-J. Yang, C.-L. Dong, Q. Hong, Q. Jiang, Z. Wang, H. Liang, Direct dioxygen radical coupling driven by octahedral ruthenium–oxygen–cobalt collaborative coordination for acidic oxygen evolution reaction, J. Am. Chem. Soc. 145 (2023) 17995–18006, https://doi.org/10.1021/jacs.3c05556.

[54] C.-Z. Yuan, S. Wang, K. San Hui, K. Wang, J. Li, H. Gao, C. Zha, X. Zhang, D. A. Dinh, X.-L. Wu, Z. Tang, J. Wan, Z. Shao, K.N. Hui, In situ immobilizing atomically dispersed Ru on oxygen-defective Co_3O_4 for efficient oxygen evolution, ACS Catal. 13 (2023) 2462–2471, https://doi.org/10.1021/acscatal.2c04946.

[55] X. Zhang, C. Wang, J. Chen, W. Zhu, A. Liao, Y. Li, J. Wang, L. Ma, Enhancement of the field emission from the TiO_2 nanotube arrays by reducing in a $NaBH_4$ solution, ACS Appl. Mater. Interfaces 6 (2014) 20625–20633, https://doi.org/10.1021/am503379y.

[56] Y. Yin, Y. Zhang, T. Gao, T. Yao, X. Zhang, J. Han, X. Wang, Z. Zhang, P. Xu, P. Zhang, X. Cao, B. Song, S. Jin, Synergistic phase and disorder engineering in 1T-$MoSe_2$ nanosheets for enhanced hydrogen-evolution reaction, Adv. Mater. 29 (2017) 1700311, https://doi.org/10.1002/adma.201700311.

[57] B. Ravel, M. Newville, ATHENA, ARTEMIS, HEPHAESTUS: data analysis for X-ray absorption spectroscopy using IFEFFIT, J. Synchrotron Radiat. 12 (2005) 537–541, https://doi.org/10.1107/S0909049505012719.

[58] G. Kresse, J. Furthmüller, Efficient iterative schemes for ab initio total-energy calculations using a plane-wave basis set, Phys. Rev. B 54 (1996) 11169, https://doi.org/10.1103/PhysRevB.54.11169.

[59] G. Kresse, J. Furthmüller, Efficiency of ab-initio total energy calculations for metals and semiconductors using a plane-wave basis set, Comput. Mater. Sci. 6 (1996) 15–50, https://doi.org/10.1016/0927-0256(96)00008-0.

[60] P.E. Blöchl, Projector augmented-wave method, Phys. Rev. B 50 (1994) 17953, https://doi.org/10.1103/PhysRevB.50.17953.

[61] J.P. Perdew, M. Ernzerhof, K. Burke, Rationale for mixing exact exchange with density functional approximations, J. Chem. Phys. 105 (1996) 9982–9985, https://doi.org/10.1063/1.472933.

[62] J.P. Perdew, K. Burke, M. Ernzerhof, Generalized gradient approximation made simple, Phys. Rev. Lett. 77 (1996) 3865, https://doi.org/10.1103/PhysRevLett.77.3865.

[63] S. Grimme, J. Antony, S. Ehrlich, H. Krieg, A consistent and accurate ab initio parametrization of density functional dispersion correction (DFT-D) for the 94 elements H-Pu, J. Chem. Phys. 132 (2010), https://doi.org/10.1063/1.3382344.

[64] H.J. Monkhorst, J.D. Pack, Special points for Brillouin-zone integrations, Phys. Rev. B 13 (1976) 5188, https://doi.org/10.1103/PhysRevB.13.5188.

[65] V.L. Chevrier, S.P. Ong, R. Armiento, M.K. Chan, G. Ceder, Hybrid density functional calculations of redox potentials and formation energies of transition metal compounds, Phys. Rev. B 82 (2010) 075122, https://doi.org/10.1103/PhysRevB.82.075122.

[66] Z. Xu, J. Rossmeisl, J.R. Kitchin, A linear response DFT+U study of trends in the oxygen evolution activity of transition metal rutile dioxides, J. Phys. Chem. C 119 (2015) 4827–4833, https://doi.org/10.1021/jp511426q.

[67] S. Ghosh, Q. Wang, G. Das, P. Jena, Magnetism in ZnO nanowire with Fe/Co codoping: first-principles density functional calculations, Phys. Rev. B 81 (2010) 235215, https://doi.org/10.1103/PhysRevB.81.235215.

Dr. Qiang Fu received his Ph.D. in Physics from Harbin Institute of Technology under the supervison of Prof. Bo Song and Prof. Xianjie Wang and subsequently carried out postdoctoral research at The Hong Kong Polytechnic University under the supervision of Prof. Jiong Zhao. His research interests center on the rational design and mechanistic understanding of transition-metal-based electrocatalysts for acidic water splitting, with an emphasis on structure–property relationships and reaction kinetics.

Dr. Lok Wing Wong is a Research Assistant Professor at The Hong Kong Polytechnic University. His research focuses on the advanced structure-property-processing relationships in low-dimensional materials, metal-organic frameworks, and covalent organic frameworks. His work utilizes (in situ) Transmission Electron Microscopy to explore their mechanical and electrical properties, catalytic performance, ferroelectricity, and methods for their synthesis and manipulation.

Prof. Xiaodong Zheng received his Ph.D. from the Institute of Metal Research, Chinese Academy of Sciences, and carried out postdoctoral research at The Hong Kong Polytechnic University under Prof. Jiong Zhao. His research focuses on two-dimensional ferroelectric semiconductors and atomic-scale mechanisms in metallic materials. He has published extensively in high-impact journals, including *Science*, *Nature Nanotechnology*, *Science Advances*, and *Nature Materials*.

Chi Shing Tsang was awarded a BS in 2021 and an MA in 2024, and he is now a PhD student in Applied Physics at The Hong Kong Polytechnic University, mentored by Prof. Zhao Jiong. His current research focuses on nanomaterials, specifically exploring ferroelectric properties in two-dimensional materials and their defects. With a background in transmission electron microscopy and material synthesis, he actively engages in collaborative research projects and has published more than 10 journal articles, including in Science, Nature Materials, Nature Nanotechnology, Nature Communications, ACS Nano, and Micro.

Honglin Chen is a PhD candidate in the Department of Applied Physics at The Hong Kong Polytechnic University, under the supervision of Prof. Zhao Jiong. His research focuses on the chemical vapor deposition of two-dimensional (2D) materials and their corresponding characterization.

Wenqian Shen received her B.S. degree from Nanjing Forestry University, Nanjing, China, in 2021, M.S. degree from Hong Kong University of Science and Technology, Hongkong, China, in 2022. Now, she is a Ph.D. student in Chemistry at City University of Hong Kong under the supervision of Prof. Ly Thuc Hue. Her research interest is focused on synthesis and characterization of 2D material.

Prof. Tao Ling is a professor at Tianjin University. His research focuses on developing novel vapor-phase metal ion exchange strategies to construct catalytic materials with hierarchical “macro–micro–atomic” multiscale architectures. By regulating active crystal facets, lattice strain, defects, and dopants, he elucidates the correlations between interfacial atomic/electronic structures and catalytic performance, overcoming limitations in activity and stability. He also designs molecular-scale reaction microenvironments at catalyst–electrolyte interfaces to enable efficient and stable natural seawater electrolysis for hydrogen production.

Prof. Thuc Hue Ly is a faculty member at City University of Hong Kong. She earned her Ph.D. in Energy Science from Sungkyunkwan University, Korea, under Prof. Young Hee Lee. Her research focuses on high-quality 2D materials, defect engineering, and their applications in electronic, optoelectronic, energy, and environmental devices. She received the NSFC Excellent Young Scientists Award (2022) and IAAM Scientist Medal (2024).

Prof. Qingming Deng is a professor at Huaiyin Normal University. His research focuses on theoretical studies of the electrical, magnetic, and mechanical properties of low-dimensional nanomaterials, including graphene, two-dimensional transition metal dichalcogenides, two-dimensional metal–organic frameworks, and one-dimensional nanowires. He also investigates the rational design of highly efficient single-atom catalysts for reactions such as CO oxidation, ORR, HER, CO_2 reduction, and ammonia synthesis, as well as the chemical properties and formation mechanisms of endohedral metal-cluster fullerenes.

Prof. Jiong Zhao is a professor in the Department of Applied Physics at The Hong Kong Polytechnic University. He received his B.S. and Ph.D. degrees from Tsinghua University in 2007 and 2012, respectively. Following postdoctoral fellowships at IFW Dresden and Sungkyunkwan University (2012–2017), he joined PolyU in 2017. Professor Zhao is a recipient of the prestigious NSFC Excellent Young Scientists Fund (Hong Kong and Macau) and the National Science Fund for Distinguished Young Scholars. His research group focuses on the growth, characterization, and application of 2D materials.